Friedrich-Alexander-Universität
Naturwissenschaftliche Fakultät

Bachelor Thesis
in Physics

Predicting Measured Stellar Flux using the Pointing Camera of CTAO's Medium-Sized Telescope

Christian Schramm

Supervisor: Prof. Dr. Christopher van Eldik

Erlangen Centre for Astroparticle Physics

Submission date: 15.07.2025

Abstract

The Medium-Sized Telescope of the Cherenkov Telescope Array Observatory (CTAO) utilizes a Pointing Camera (PCAM) to enhance its pointing accuracy by matching the observed night sky to the catalogued data. This thesis uses the measured intensities and the data of the fitted stars to quantify different effects in the atmosphere, aiming to predict the measurable flux of a given star and investigating whether the images taken by PCAM can be used to quantify the atmospheric quality.

Using the star's magnitude, temperature and position on the sky, effects like the wavelength dependent detection efficiency of the camera, the zenith distance and wavelength dependent atmospheric extinction as well as systematic errors by the extraction algorithm, are quantified. By analysing data taken at different altitudes, atmospheric parameters like the extinction coefficient and the Ångström-exponent are determined for the night and location of the campaign.

The intensity prediction allows for an additional validation and correction for the pointing algorithm. Deviations from the predictions point to wrong star fitting or atmospheric effects like clouds. A systematic underestimation of the intensity is hypothesized to be caused by interstellar reddening of the star spectra, which is not yet corrected for in the wavelength dependent predictions.

This presented method provides a foundation for an automated quality control of the sky fitting and the measurements of atmospheric conditions at the site of CTAO.

Contents

1 Introduction and Motivation **1**

1.1 Gamma Ray Astronomy and CTAO 1

1.2 The Pointing of MST 3

1.2.1 The Pointing Camera 3

1.2.2 Sky Fitting 5

1.3 Motivation for Predicting the Measured Stellar Flux 6

2 Used Parameters **7**

2.1 Magnitude, Flux and Temperature 7

2.2 Blackbody Radiation 7

2.3 Mean Wavelength 8

2.4 Night Sky Campaigns 10

3 Effects on the Measured Intensity **11**

3.1 The Extraction Algorithm 11

3.2 Detection Efficiency 15

3.3 Extinction Equation 18

3.3.1 Calculating the Airmass 18

3.3.2 Extinction Coefficient τ 21

3.3.3 Extra Terrestrial Flux I_0 23

4 Predicting the Measured Star Intensity **25**

4.1 Interstellar Reddening 26

4.2 Removing Badly Fitted Stars 29

5 Summary and Outlook **31**

A Appendix **35**

Bibliography **43**

Declaration of originality **45**

1 Introduction and Motivation

1.1 Gamma Ray Astronomy and CTAO

The most energetic environments in the universe, like Active Galactic Nuclei (AGN) or supernovae, are able to accelerate charged particles to relativistic speeds with energies up to 10^{20} eV. These cosmic rays interact with the Interstellar Medium (ISM) among others, by inverse Compton scattering and π^0-production. During these processes, gamma rays are produced with energies of up to multiple TeV. These gamma rays are excellent messengers as they are not influenced by magnetic fields (CTAO, 2025b). As this helps to get a deeper understanding of the universe and to explore the current scientific limits, gamma ray astronomy has resulted in multiple gamma ray detectors being built. The current generation of ground based detectors like High Energy Stereoscopic System (H.E.S.S.), Major Atmospheric Gamma Imaging Cherenkov Telescope (MAGIC) or Very Energetic Radiation Imaging Telescope Array System (VERITAS) have identified over 200 gamma ray sources and proved the potential of this field. The planned Cherenkov Telescope Array Observatory (CTAO) is building on these successes and will be the most advanced array of its kind. The detection principle of all ground-based gamma ray observatories is based on the measurement of Cherenkov light produced by a gamma ray.

When gamma rays hit Earth's atmosphere, they initiate a cascade of subatomic charged particles, known as an extensive air shower, which are energetic enough to travel faster than light in the atmosphere. Any charged particle, moving through a medium, polarizes the particles of the medium around its travel path, which in response re-emit the received energy as photons as they return to their ground state. The polarization field, and thereby the emitted photons, form spherical, symmetrical wavefronts around the moving particle as long as it is moving slower than the wavefronts themselves ($v_p < c_n$ where $c_n = c_0/n$ is the speed of light in the medium). As soon as a particle is moving

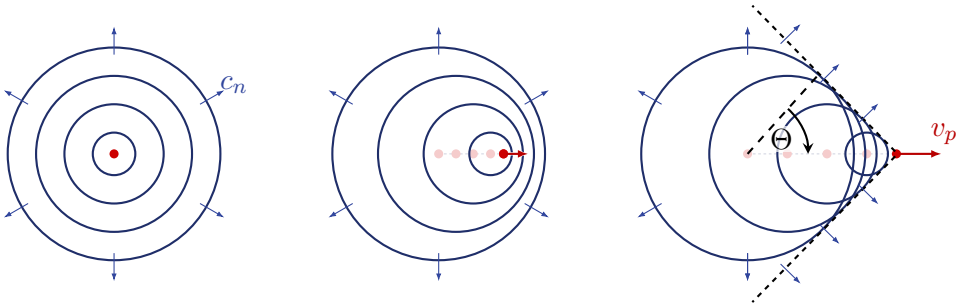

Figure 1: Sketch of Cherenkov light production. From left to right: $v_p = 0$, $0 < v_p < c_n$, $v_p > c_n$. Adapted from Neutelings (2025).

faster than the phase velocity of light, like the ones emitted in a gamma ray induced atmospheric air shower, it can catch up with, or even overtake, its own produced wavefronts (see Figure 1). This results in the emitted wavefronts overlapping and constructive interference, producing a cone of observable photons around the particle's flight path. This signal is called Cherenkov light and can be measured using suitable instruments.

The emission angle Θ at which the Cherenkov light is produced depends on the speed of the particle $\beta = v_p/c_0$, the refraction index of the medium n (see Figure 1) and is given by

$$\cos(\Theta) = \frac{c_n}{v_p} = \frac{1}{n\beta}. \tag{1}$$

By detecting the signal of the Cherenkov event with at least two telescopes and measuring the signal form and time of arrival, it is possible to triangulate the position, entry angle, and emission angle of the light cone (see Figure 2). This allows the reconstruction of

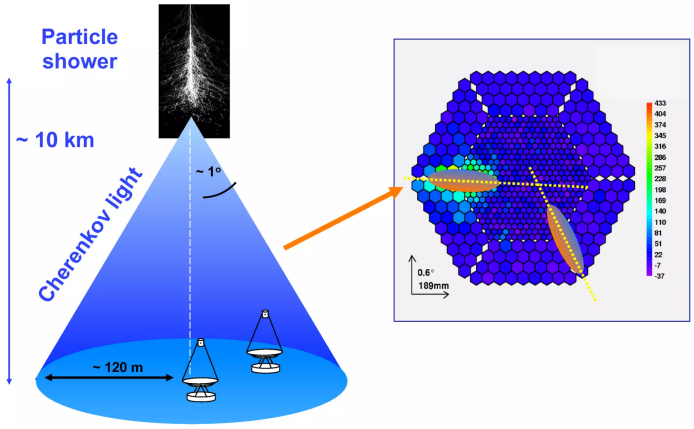

Figure 2: Sketch on how to triangulate the shape of a Cherenkov Light cone using two Cherenkov telescopes. Taken from Schweizer (2025).

the particle's velocity and path, and based on this, the modelling of the original gamma rays' energy and origin.

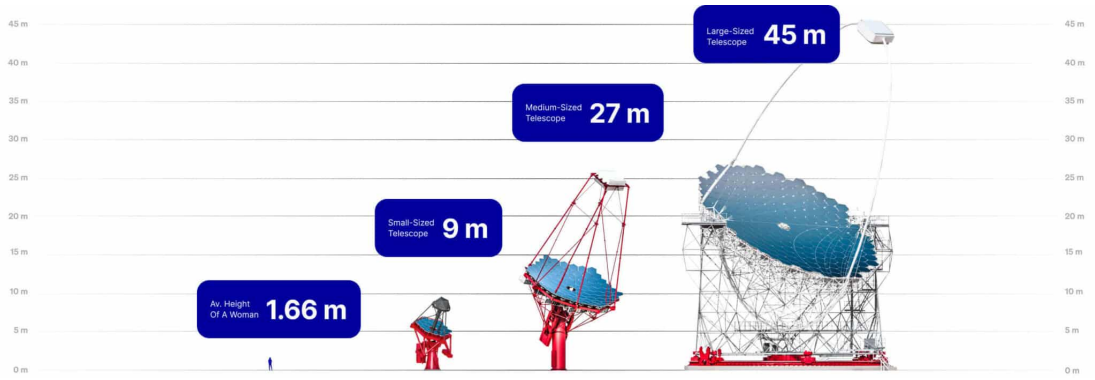

Figure 3: Comparing the size of the three different telescope types used in CTAO. Taken from CTAO (2025a).

The CTAO is designed as the next generation of such observatories. It will offer unmatched angular resolution, sensitivity and energy coverage, setting new standards in this field. To achieve a broad detectable energy range between ($\sim 20\,\mathrm{GeV}$ and $300\,\mathrm{TeV}$) CTAO will cover an area of over $1\,\mathrm{km}^2$ with three different types of telescopes. The most frequent low energy range ($20\,\mathrm{GeV}$ to $150\,\mathrm{GeV}$) gamma rays produce fewer secondary particles which results in less Cherenkov light and thereby a lower intensity flash that

can be detected. This is why the Large-Sized Telescopes (LSTs) of CTAO, that cover this range, are fewer in number but greater in size to detect even the faintest light flashes. In contrast, gamma energies in higher ranges (5 TeV to 300 TeV) are less common but produce stronger air showers with higher Cherenkov intensities. As a result Small-Sized Telescopes (SSTs) are enough to detect these events but need to cover as large an area as possible to increase the chance of detecting as many as possible. In the range between the already named energy ranges (150 GeV to 5 TeV) act the Medium-Sized Telescopes (MSTs). (CTAO, 2025a)

1.2 The Pointing of MST

The MSTs are planned to observe gamma rays with an energy range of 150 GeV - 5 TeV at a pointing precision of < 7 arcsec. To achieve this precise orientation of a 27 m high structure that has a camera placed 16 m away from its mirrors (see Figure 4), one cannot only rely on the mechanisms that move it there (CTAO, 2025a). To compensate for pointing errors due to tolerances, wear in the mechanics, calibration errors, or thermal contraction/expansion of the structure, a pointing camera is placed inside the centre of MST's dish, aligned with the telescope's optical axis observing the science camera and the night sky behind.

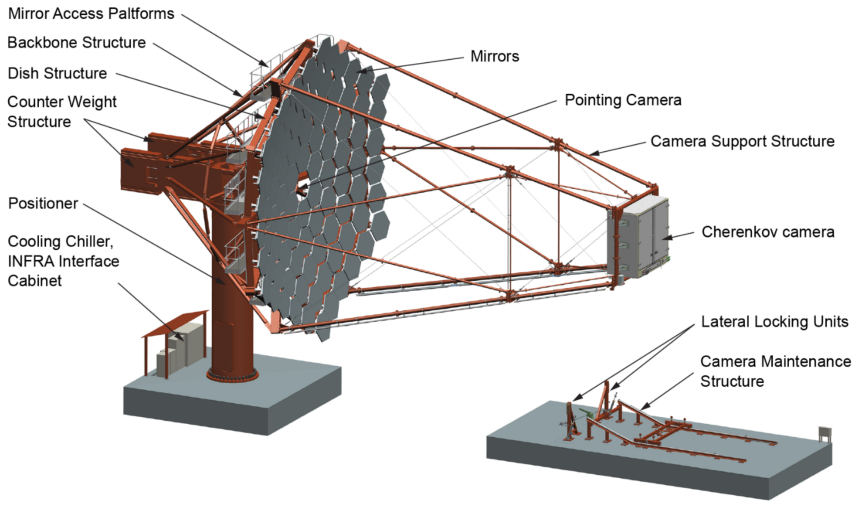

Figure 4: Design of the Medium-Sized Telescope with labels. Taken from Garczarczyk (2022).

1.2.1 The Pointing Camera

The Pointing Camera (PCAM) consists at its core of the optical astro camera ZWO ASI2600-MM Pro with a chip size of 6248×4176 pixels, distributed over an area of 23.5×15.7 mm. Directly behind the chip is a thermally connected chip cooling unit, to reduce dark current (ECAP, 2022). Attached to the front of the camera is the lens Nikon AF NIKKOR 50mm 1:1.8 D, which focuses the incoming light on the sensor. This lens can additionally be heated to correct for possible thermal fluctuations that

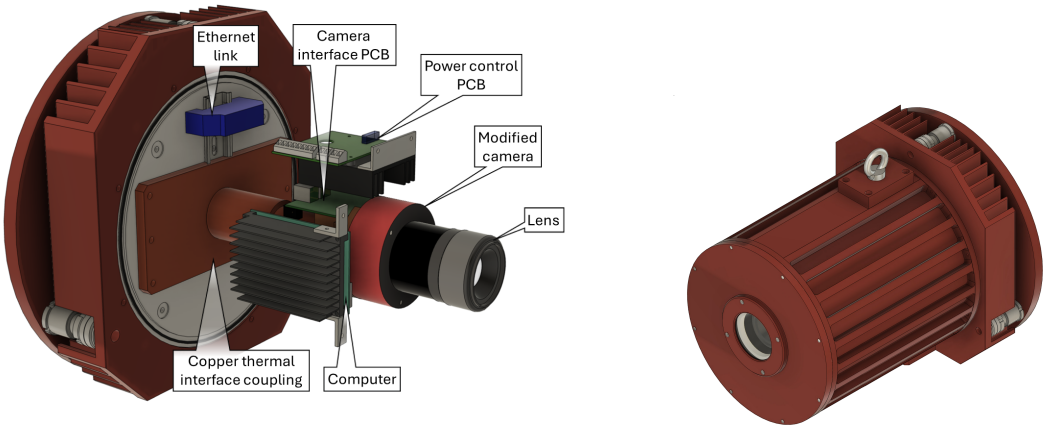

Figure 5: CAD 3D model of the PCAM interior and housing. Taken from Matzke (2024).

would influence the optics. Around the whole camera setup, an aluminium housing is placed that is not only used for mechanical stabilisation, but also thermally connects to every major heat source of the setup, to passively transfer the heat to the surroundings. In the front of the housing a glass window is mounted as such that the camera's FoV is not impaired. A 3D model of the inside and the housing of the PCAM, is seen in Figure 5.

The camera is designed to capture visible wavelengths within a range of around 300 nm to 700 nm, with its efficiency peak at ~ 500 nm. The sensitivity curve over specific wavelengths is graphically given in the data sheet of ZWO ASI2600-MM Pro (Suzhou ZWO Co, 2025) and can be extracted and interpolated by an online tool like `graphreader.com` (Larsen, 2025).

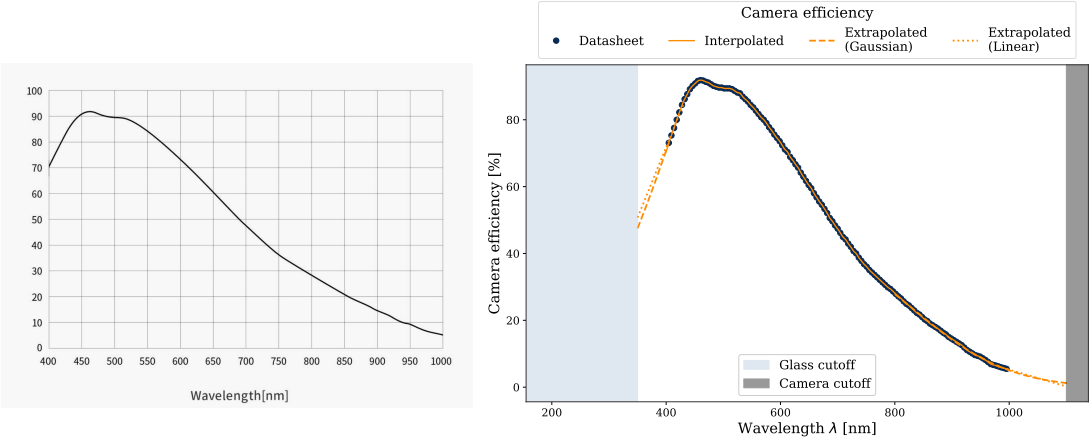

(a) Data provided by data sheet of Suzhou ZWO Co (2025).

(b) Extracted, inter- and extrapolated data, with set lower and upper cut-off.

Figure 6: Camera sensitivity of ZWO ASI2600-MM Pro.

Since the data sheet only provides values between 400 nm and 1000 nm, but light also reaches the sensor with wavelengths outside this range, the curve is extrapolated. This is done once using a linear fit and once with a Gaussian fit for the lower and upper data points (see Figure 6b). The resulting deviation between both approaches is later used as the systematic error.

The wavelength at which the linear extrapolation on the right side crosses the x-axis ($\lambda \approx 1101$ nm) is taken as an upper limit of the detection range, above which the camera is estimated to not detect any events (see grey area in Figure 6b). The lower end of the efficiency curve is limited by the glass in front of the sensor (inside the lens and the glass panel of the housing). Standard soda lime silica glass (like the glass panels of windows) is effectively impervious to wavelengths roughly below 350 nm or above 5000 nm (Rubin, 1985), which is why it is assumed that no wavelengths in that range are reaching the camera and the lower cutoff is set to 350 nm (see blue area in Figure 6b).

1.2.2 Sky Fitting

With a FoV of around 27°×18°, the Pointing Camera is able to view the science camera as well as the night sky behind it. 12 LEDs arranged in a circle around the science camera are used to reconstruct the position of it within the frame and its distance from the dish. By fitting the positions of stars within the FoV of the camera, the exact pointing of the setup can be calculated (Matzke, 2024).

For the pointing reconstruction, the PCAM takes a 10 s image every 10 s to 60 s of its FoV. To solve this image, first all spots (pixels with intensities over a set threshold) outside the Cherenkov camera are extracted. By connecting the 15 brightest of the extracted spots in all possible groups of three, the algorithm gets a list of triangles (called quads) with different geometrical properties, like side lengths or interior angle composition.

By providing the algorithm a pointing estimation of the camera, it is able to pull the already solved quads of the brightest 100 stars in a range of ±1° outside the estimated FoV from an available catalogue (like Gaia Collaboration et al. (2025)). This information is then fitted together (using a χ^2 fit) until the best combination is found. By extracting the positions of the solved quads, the system can now reconstruct the position of all spots/stars in the picture and, as a result, the camera pointing. After checking the positional deviations of each star, and removing wrongly fitted stars, the fit is iteratively done again until a sufficient fit quality is achieved.

As soon as each spot is paired with a corresponding star, more properties of these stars can be extracted out of the star catalogues for later use, like the star's magnitude, effective temperature, distance, or any other variable available in the catalogue provided by the Global Astrometric Interferometer for Astrophysics (Gaia) (Documentation of `cta-pointing` package by van Eldik (2025)).

1.3 Motivation for Predicting the Measured Stellar Flux

The solving algorithm for the night sky depends strongly on the correct detection of stars in the image. By introducing spots to the image that are wrongly detected as stars, such as slowly moving asteroids or satellites, dead pixels of the camera, galaxies, planets, or other small but bright objects, some quads may be produced including these objects instead of real stars. This reduces the number of fitted actual stars and the quality of the fit. As a result, the pointing accuracy decreases.

If the expected measured flux of a star can be predicted, this could be compared to the actually detected intensity to get an additional quality check (in addition to the comparison of detected vs. expected positions) if the stars are fitted correctly. This should in effect improve the fitting and pointing.

Another use for the prediction of a star's intensity is the analysis of the local atmospheric conditions at the time of measurements. As the measured intensity should depend on its wavelength and the extinction of the atmosphere, one could conclude how many and what kind of particles are in the air or just where in the image clouds are located. This can once again be useful for the solving process, as high cloud coverage influences the number of visible stars up to a point where the pointing is unable to produce reasonable solutions.

2 Used Parameters

Prior to the actual quantification of the processes a light ray has to go through, a few important variables are defined in this chapter.

2.1 Magnitude, Flux and Temperature

The flux of a star I is measured in arbitrary units [arb. units], which correspond to the detected photon count on a given pixel and is thereby proportional to the deposited energy of the photon. As the magnitude of a light source is defined by the logarithmic intensity, the intensity can be expressed by the magnitude m using (Demtröder, 2017)

$$I \propto 10^{-m/2.5\,\mathrm{mag}}. \tag{2}$$

The star's magnitude m [mag] is obtained from the Gaia catalogue for the solved stars. Gaia's apparent magnitude values are detected by satellite and catalogued without any further corrections for ISM or distances. The magnitudes are available in the bandwidths BP (∼330-680 nm), RP (≈630-1050 nm) and the combined range G (≈330-1050 nm) produced by combining both bandwidths. In this thesis, the G-magnitude is used, as it covers most of our camera's detection range estimated in subsection 1.2 (350-1101 nm). **The effective star temperature T_{eff}** [K] is also extracted out of the Gaia-catalogue. Gaia estimates this star-surface-temperature for a number of stars by interpreting their received spectrum and correcting for distance and interstellar effects. (Gaia Collaboration et al., 2025)

2.2 Blackbody Radiation

The blackbody spectrum describes the expected flux at discrete wavelengths and is calculated by Planck's law using:

$$w_\lambda(\lambda, T) = \frac{8\pi hc}{\lambda^5} \frac{1}{e^{hc/(\lambda k_B T)} - 1}. \tag{3}$$

Where the spectral energy distribution w_λ at wavelength λ for a blackbody at temperature T is calculated using the speed of light c, the Planck constant h and the Boltzmann constant k_B. (Demtröder, 2016)

As seen in Figure 7, a changing BB temperature does not only affect the intensity's amplitude, but also the location of its peak. The position of the peak intensity follows Wien's law ($\lambda_{\mathrm{peak}} \propto T^{-1}$) (Demtröder, 2016). Hotter stars, therefore, dominate in shorter wavelengths and appear blue, while a colder star's spectrum appears more red, as it is located in longer wavelengths.

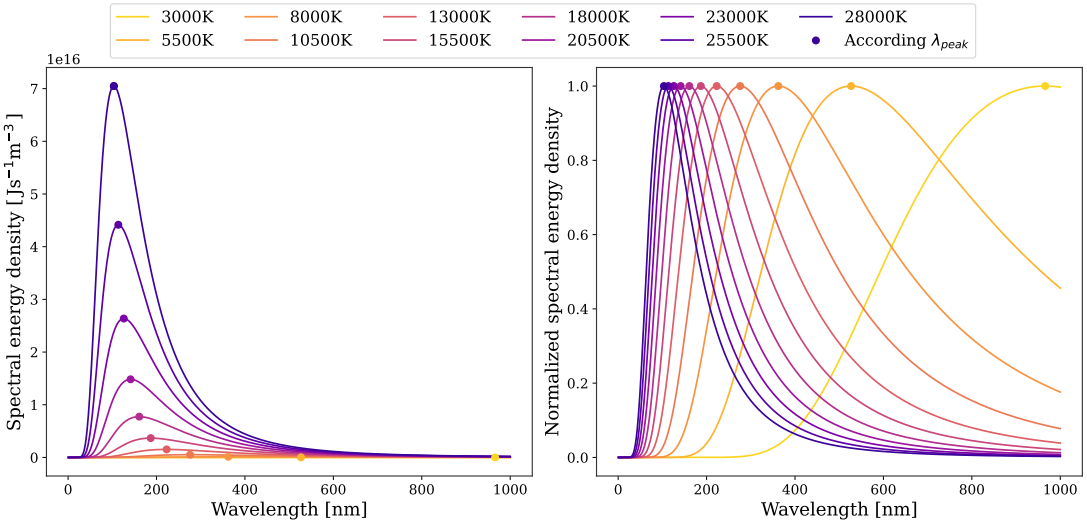

Figure 7: The spectrum of a blackbody radiator at different temperatures (left) and the same normalized by the maximum value (right). Dots: corresponding peak wavelengths, according to Wien's law.

2.3 Mean Wavelength

The mean wavelength $\bar{\lambda}$ is a quantity used as a representative value for a star's spectrum. Because many effects covered later in this thesis are wavelength-dependent and the calculation of the impacts on the whole spectrum range would often exceed the scope of this bachelor's thesis, the spectrum needs to be focused on a single value. The peak wavelength of the spectrum is not a reasonable choice, since the detection range limits what wavelengths we can inspect, and λ_{peak} frequently lies outside this range. By using the peak wavelength, we would quantify the dependencies based on a wavelength which is not measured and therefore distort the results.

A reasonable compromise is to calculate the mean wavelength inside the detection range weighted by the blackbody spectrum. This is realized by dividing the integrated weighted spectrum by the integral of the unweighted spectrum inside the range:

$$\bar{\lambda} = \frac{\int_{350\,\text{nm}}^{1101\,\text{nm}} \lambda\, w_\lambda(\lambda, T)\,\mathrm{d}\lambda}{\int_{350\,\text{nm}}^{1101\,\text{nm}} w_\lambda(\lambda, T)\,\mathrm{d}\lambda}. \tag{4}$$

For simplification, this is done numerically in `Python` for 1000 different blackbody temperatures between 500 K and 60000 K. This is further interpolated in Figure 8, to get a result for every star temperature.

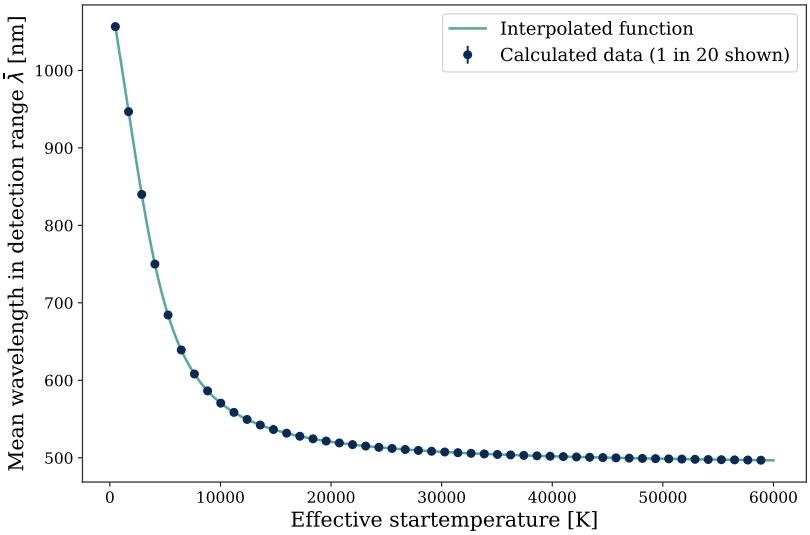

Figure 8: Calculated mean wavelength in range 350 nm to 1101 nm of blackbody radiators at different temperatures with interpolated function. For better visibility only every 20th point plotted (50 out of 1000).

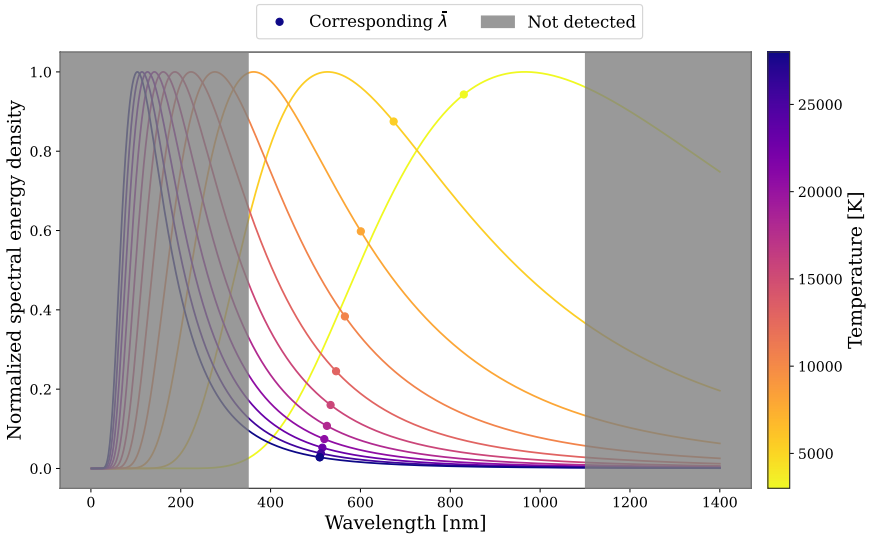

Figure 9: Normalised blackbody spectrum, with marked positions of the corresponding mean wavelengths and borders of the detection range.

To get a better idea of where the calculated mean wavelengths lie in respect to their spectrum, the normalised blackbody spectra are once again plotted for different temperatures in Figure 9. On top, the borders of the detection range as well as the spectral values at the mean wavelengths, are plotted.

It is important to mention that we estimate the received spectrum by the original blackbody spectrum of the star, based on its surface temperature. However, between the star and the PCAM lie the Interstellar Medium and the atmosphere. Depending

on its wavelength, a photon is absorbed to different extents. A long wavelength is able to penetrate different media more easily than its shorter counterpart. This results in the blue parts of the spectrum getting reduced more strongly and the whole spectrum shifting towards longer wavelengths. The amount of this interstellar reddening is highly dependent on the galactic direction being observed and the distance to the star (Fitzpatrick, 1998). As the calculations required to correct the spectrum for the reddening exceed the scope of a bachelor's thesis, this is not considered in this work. To get more accurate results, this could be approached in a future work.

2.4 Night Sky Campaigns

The processed data in this thesis was taken in two night sky campaigns. The first one was done on March 17 of 2025, on the rooftop of the Erlanger Centre of Astroparticle Physics (ECAP) (between 18:22 UTC and 03:58 UTC), with a continuous camera pointing at an altitude $\approx 65.51°$, azimuth $\approx 1.95°$. Due to its continuous nature, it will be referred to as the Continuous Campaign.

In contrast stands the Pointed Campaign that was taken on the 20th of March 2025 between 19:12 UTC and 20:16 UTC. This campaign was also conducted on the ECAP rooftop, but manually pointed to 40 different altitude/azimuth positions to cover a greater range of pointing positions.

3 Effects on the Measured Intensity

To accurately predict the intensity displayed on the screen for a given star, one first has to understand the photon's path to the observer and what effects acted on it and to what extent.

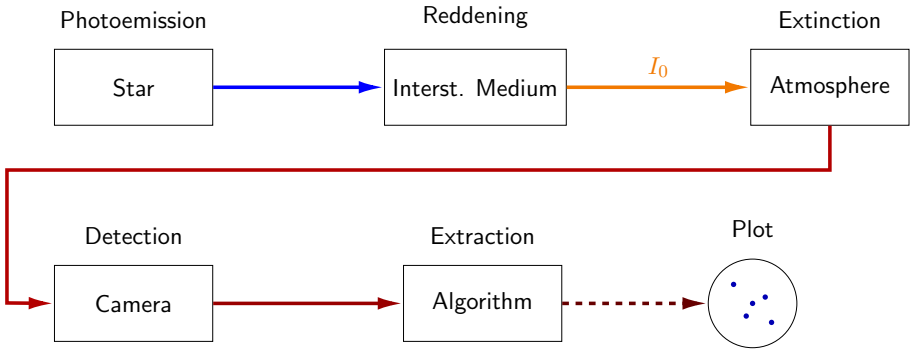

Figure 10: A photon's path from its source to the final plot on the computer.

A simplified path of a light ray from a star to the display is sketched in Figure 10. A photon is emitted by a star at a spectrum described by Planck's law for blackbody (BB) radiators. It travels through the Interstellar Medium (ISM), where it loses, wavelength dependent, some of its energy, which results in a spectral shift. Arriving at Earth's atmosphere the ray has the intensity I_0. As it travels through the atmosphere, it again is partially absorbed, before it enters the PCAM where it gets detected according to the camera's efficiency before its flux is digitally extracted.

To model all these effects, this chapter will cover the influences on the star light in reversed order starting at the spot extraction algorithm. This way we are trying to quantify each influence so that in the end a star's measured flux can be sufficiently explained and predicted.

As explained in section 2 we would expect all measured intensities to precisely follow an exponential relation with the corresponding magnitudes.

$$I(m) = A \cdot 10^{-m/2.5\,\mathrm{mag}}, \tag{5}$$

with the proportionality factor A.

By taking a look at the data of the uncorrected Continuous Campaign in Figure 11 and fitting Equation 5 to the points, it is clear that this does not represent the data sufficiently. While one could argue that the data still follows the expected slope in the lower magnitudes ($m \lesssim 6.5\,\mathrm{mag}$), from 7.5 mag onwards, they start increasingly spreading and at the same time dropping below the fit.

3.1 The Extraction Algorithm

To inspect the influence the extraction algorithm has on the final data, a 10 s exposure of the night sky without atmospheric influences is simulated at right ascension = 37°

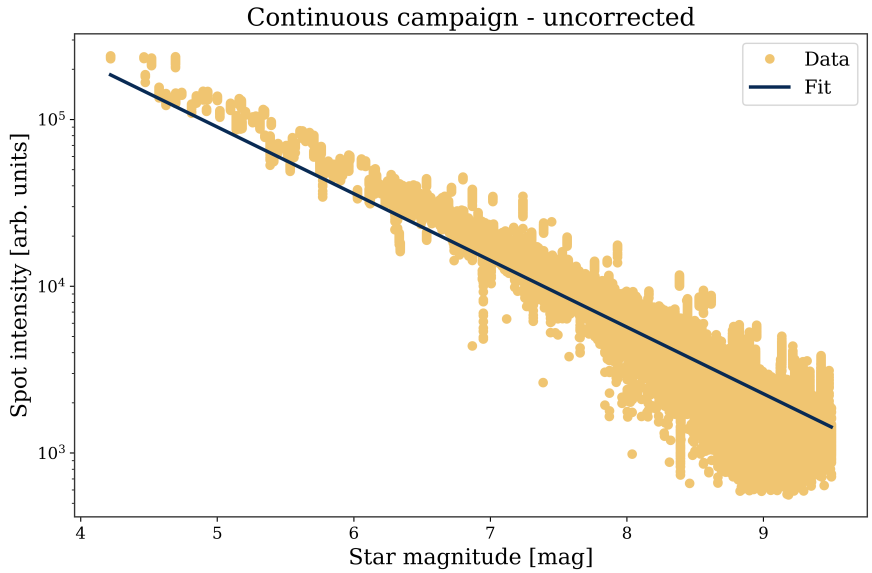

Figure 11: Uncorrected data of Continuous Campaign with intensity-magnitude fit.

and declination = 90°. While the spread is reduced to a minimum, the drop-off at higher magnitudes becomes even more visible. By changing the detection threshold to different values (see Figure 12), it becomes obvious that this is an effect of the extraction algorithm.

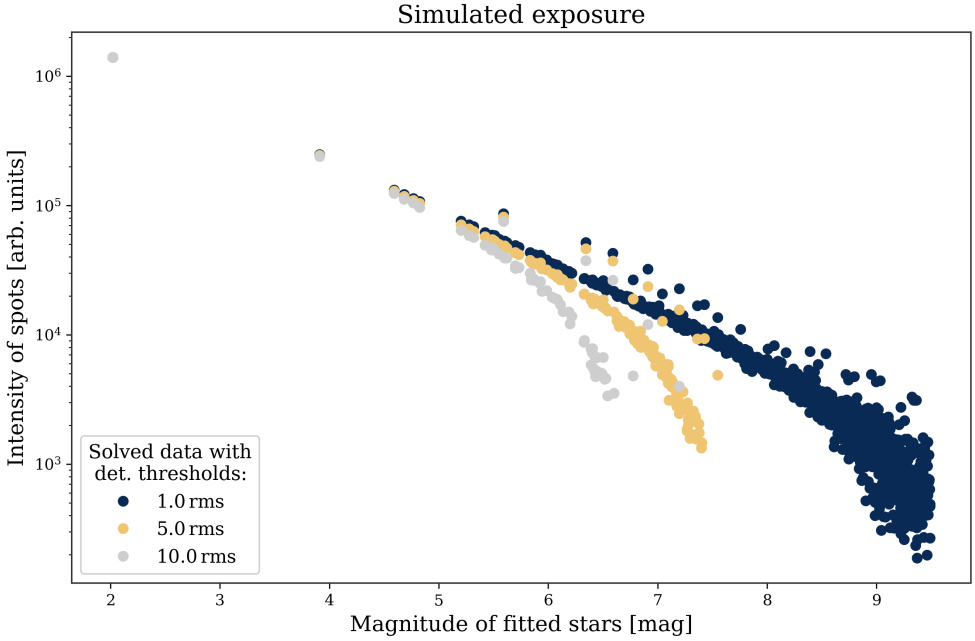

Figure 12: Simulated and solved exposure (RA = 37°, DEC = 90°) with different detection thresholds in multiples of the background RMS.

This can be explained by taking a closer look at the principles of the extraction process

and the form of each spot. Each star produces a 2-dimensional Gaussian distribution on the chip due to atmospheric scattering and an unfocused camera (see Figure 13):

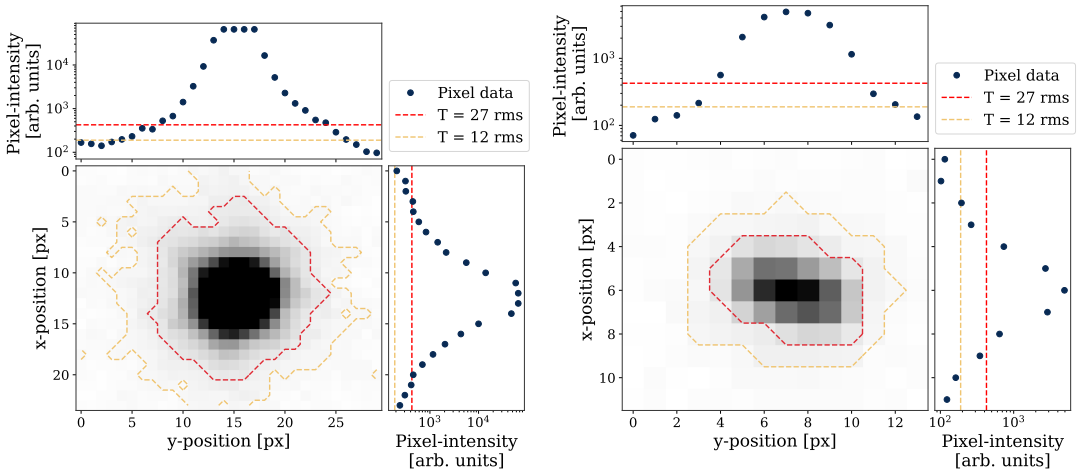

(a) Brightest found star

(b) Dimmest found star

Figure 13: Intensity distribution of single stars on the pixel plane of the camera. In red/yellow: high/low detection threshold in multiples of the background RMS intensity.

$$I(x, y) = I_{\text{peak}} \cdot e^{-\frac{x^2+y^2}{2\sigma^2}}, \tag{6}$$

with the intensity of the brightest pixel in the centre I_{peak}, the x and y distance to the centre and the width of the distribution σ.

In polar coordinates, this can be written as

$$I(r) = I_{\text{peak}} \cdot e^{-\frac{r^2}{2\sigma^2}}, \tag{7}$$

with the distance to the centre $r = \sqrt{x^2 + y^2}$.

The detection-threshold governs which pixels are counted as a part of the star, without influencing the single pixel's intensity. A higher T-value does, thereby, decrease the width of the extracted spot r_T and the number of detected spot-pixels. This in effect reduces the integrated flux. An expression for r_T is achieved by calculating where the intensity drops to the chosen threshold:

$$T = I(r_T) = I_{\text{peak}} \cdot e^{-\frac{r_T^2}{2\sigma^2}} \Rightarrow e^{-\frac{r_T^2}{2\sigma^2}} = \frac{T}{I_{\text{peak}}}. \tag{8}$$

The integrated flux I_r up to a specific point is predicted by

$$\begin{aligned} I_r = \int_0^{2\pi} \int_0^r I(r)\, \mathrm{d}r\mathrm{d}\vartheta &= 2\pi I_{\text{peak}} \int_0^r r e^{-\frac{r^2}{2\sigma^2}}\, \mathrm{d}r \\ &= 2\pi\sigma^2 I_{\text{peak}} \left(1 - e^{-\frac{r^2}{2\sigma^2}}\right). \end{aligned} \tag{9}$$

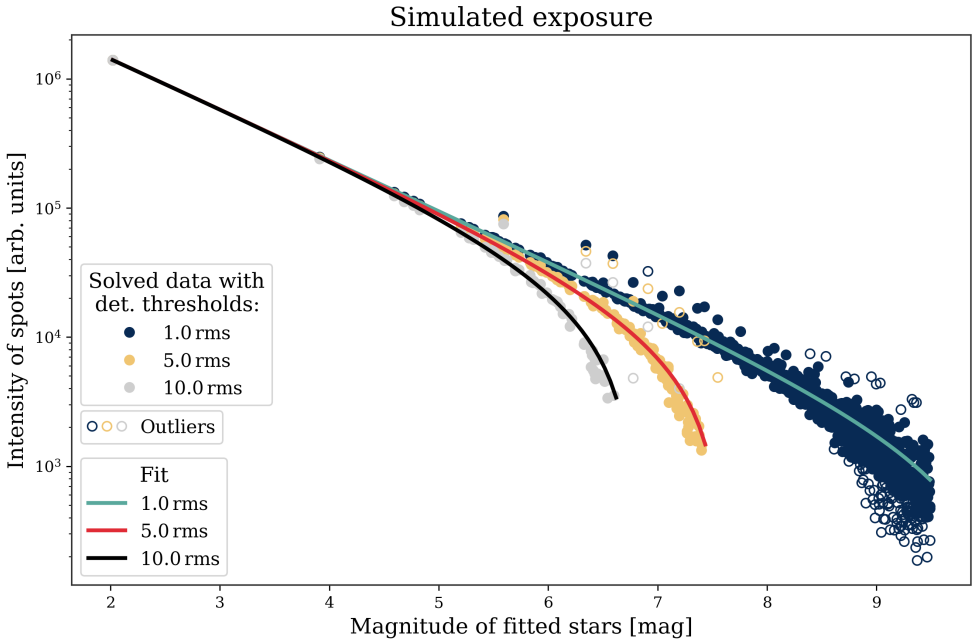

Figure 14: Fitted intensity curve on extracted and solved stars out of simulated exposure. Fitted parameters can be found in appendix A.2.1.

Which results in the expected total intensity of the star

$$I_{\text{tot}} = I_{r\to\infty} = 2\pi\sigma^2 I_{\text{peak}}$$

and the expected extracted intensity up to r_T

$$I_{\text{extr}} = I_{r_T} = 2\pi\sigma^2 I_{\text{peak}} \left(1 - e^{-\frac{r_T^2}{2\sigma^2}}\right).$$

The percentage of flux that is extracted above T should thereby follow

$$\eta_{\text{extr}} = \frac{I_{\text{extr}}}{I_{\text{tot}}} = \left(1 - e^{-\frac{r_T^2}{2\sigma^2}}\right) \overset{(8)}{=} 1 - \frac{T}{I_{\text{peak}}}. \tag{10}$$

In Equation 10 it becomes clear why the extracted intensity drops faster for darker stars than for brighter ones, since the percentage of extracted flux decreases the dimmer the star gets (smaller I_{peak}). As I_{peak} is not affected by the threshold, it is proportional to $I_{\text{tot}} \propto 10^{-m/B}$. Therefore, the extracted intensity takes on the form of

$$\begin{aligned} I_{\text{extr}} &= I_{\text{tot}} \left(1 - \frac{T}{I_{\text{peak}}}\right) = I_{\text{tot}} - \frac{T \cdot I_{\text{tot}}}{c \cdot I_{\text{tot}}} \\ \Rightarrow I_{\text{extr}} &= A \cdot 10^{-m/B} - C, \end{aligned} \tag{11}$$

with $I_{\text{peak}} \propto I_{\text{tot}} \propto 10^{-m/B}$ and the proportionality factors A and c, respectively $C = T/c$.

To fit Equation 11 to the intensity curves of the extracted stars as seen in Figure 14, the fit is done twice. The first one is used to filter out every star that lies more than 2σ

outside this first fit (see Outliers in Figure 14). The second fit is then done using only the remaining stars. All fit values can be found in appendix A.2.1. The fitted B-values, are on average (2.57 ± 0.05) mag, which lies within 2σ of the theoretical value 2.5 mag. The fitted value A is a quantity that describes the intensity of a reference star at 0 mag, in addition to any systematic offset and averages in our fits to around $(8.60 \pm 0.28) \times 10^6$ arb units. The C-values should be proportional to the threshold T, which does seem true comparing $C_{5\text{rms}} = (9.53 \pm 0.15) \times 10^3$ arb units and $C_{10\text{rms}} = (21.12 \pm 0.52) \times 10^3$ arb units, where $C \approx 2 \cdot T$, while $C_{1\text{rms}} = (0.91 \pm 0.03) \times 10^3$ arb units deviates from that trend. The reason for this probably being the higher quantity of extracted spots and the resulting higher spread in higher magnitude ranges. As a threshold of 5 rms is used for future extractions, a C-value of around 9.5 arb. units is expected.

To compensate for this now quantifiable effect, Equation 11 is used to calculate the camera detection efficiency

$$\eta_{\text{extr}}^{-1} = \frac{I_{\text{tot}}}{I_{\text{extr}}} = 1 + \frac{C}{I_{\text{extr}}}.$$

Comparing the data of a real campaign with and without this correction (Figure 15), the removed dropoff at higher magnitudes becomes clear by inserting the same linear

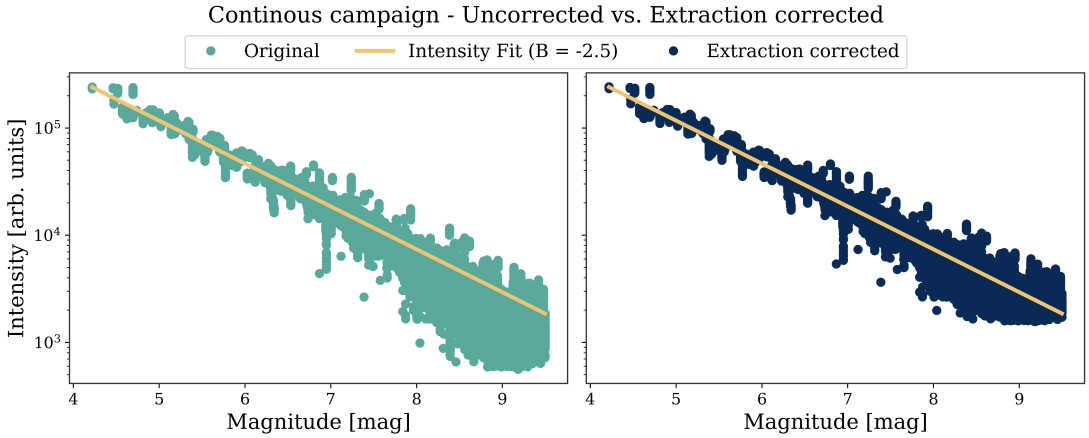

Figure 15: Comparison of the uncorrected (left) and the extraction drop-off corrected (right) data points (ECAP-rooftop: pointed-campaign 20th march 2025). Included the same (to the corrected data) fit function in both plots for better comparison.

fit ($I = -\frac{\log(m)}{2.5\,\text{mag}} + \log(A)$) into both datasets. While the original plot follows the line only up to ~ 7 mag and starts dropping off after that, the corrected data points stay symmetrically distributed around the fit.

This correction is done for the data of all remaining chapters.

3.2 Detection Efficiency

Before the intensity can be extracted by the algorithm described earlier, it has to first be detected by the camera setup. The camera setup consists - reduced to the beam path - of the astro camera ASI2600-MM Pro containing the sensor, the lens Nikon AF

NIKKOR 50mm 1:1.8 D to focus the incoming light on the sensor, and an additional glass panel of the camera housing. This chapter will inspect how the setup influences the detected flux and how to correct for possible wavelength dependencies.

The camera sensor itself is optimized for visible light (380 nm-780 nm), although not uniformly sensitive at different wavelengths. The wavelength-dependent camera detection efficiency can be extracted and interpolated out of its data sheet (Suzhou ZWO Co, 2025) using an online tool like `graphreader.com` (Larsen, 2025). As this only provides data from 400 nm to 1000 nm, but stellar radiation spans a wider range, the curve is extrapolated further. This is done once using a linear fit and once with a Gaussian fit for the lower and upper data points (see Figure 16). The resulting deviation between both approaches is later used as the systematic error.

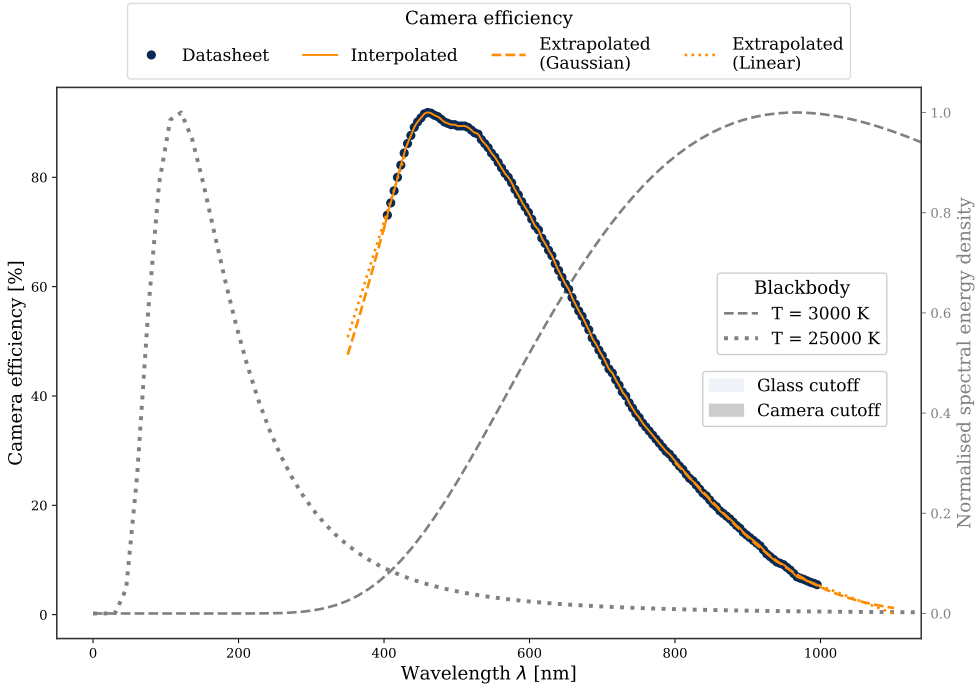

Figure 16: Camera efficiency (Darkblue dots: Extracted from datasheet (Suzhou ZWO Co, 2025), Orange solid line: Interpolated function between data, Orange dashed line: extrapolated Gaussian-fit, Orange dotted line: Extrapolated linear-fit. Normalised blackbody radiation in Grey for different temperatures. Cutoff after which no detection is expected: Light-Blue due to glass in front of camera, Grey due to extrapolated camera efficiency. Fitted parameters in appendix A.2.2.

The wavelength at which the linear extrapolation on the right side crosses the x-axis ($\lambda \approx 1101$ nm) is taken as an upper limit of the detection range, above which the camera is estimated to not detect any events (see grey area in Figure 16). The lower end of the efficiency curve is limited by the glass in front of the sensor (inside the lens and the glass panel of the housing). Standard soda lime silica glass (like the glass panels of windows) is effectively impervious to wavelengths roughly below 350 nm or above 5000 nm (Rubin, 1985), which is why it is assumed that no wavelengths in that range are reaching the camera and the lower cutoff is set to 350 nm (see blue area in Figure 16).

As discussed in section 2 does the effective temperature of a star strongly influence at which wavelengths more or less photons are emitted. This results in the peaks of the spectra shifting from far infrared ($\approx 1450\,\text{nm}$ at $2000\,\text{K}$) to ultraviolet ($\approx 65\,\text{nm}$ at $45\,000\,\text{K}$) ranges (Demtröder, 2016), which strongly affects how much of a star's intensity lies within the detection range. Additionally, the spectral shift influences what parts of the spectrum overlap with which camera efficiency. For visualization, the black body spectrum at $T = 3000\,\text{K}$ and $T = 25\,000\,\text{K}$ is plotted, normalized by the according peak energy density, in Figure 16.

To equalize the spectral dependence of the measured intensity, the ratio between the expected detected intensity and the theoretical total spectral energy is calculated for different blackbody temperatures. I_{in} hereby represents the total radiation emitted in the sensitive range. I_{det} is the portion that actually is detected by the camera, weighted by the efficiency curve.

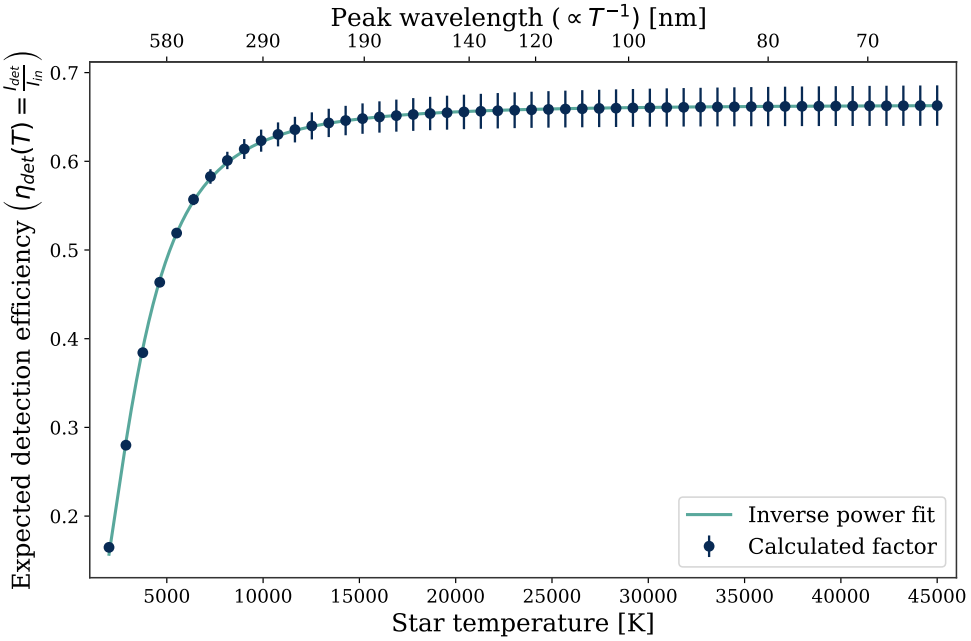

Figure 17: Plotted and fitted detection efficiency for the spectra of stars with effective temperatures between 2000 K and 45000 K, with the corresponding peak wavelength on top. Fitted parameters in appendix A.2.2.

While the theoretical incoming energy can be calculated just by integrating Planck's law between the two cut-offs:

$$I_{\text{in}} = \int_{350\,\text{nm}}^{1101\,\text{nm}} w_\lambda(\lambda)\mathrm{d}\lambda \tag{12}$$

I_{det} is calculated by correcting Planck's law with the corresponding camera efficiency before integrating it:

$$I_{\text{det}} = \int_{350\,\text{nm}}^{1101\,\text{nm}} w_\lambda(\lambda) \cdot \eta_{\text{cam}}(\lambda)\mathrm{d}\lambda. \tag{13}$$

As there is no analytical equation for the camera efficiency η_{cam}, both integrals are done numerically. After plotting the resulting detection efficiency $\eta_{\text{det}}(T) = I_{\text{det}}/I_{\text{in}}$

and fitting an inverse power function of the form

$$\eta_{\text{det}}(T) = \frac{1}{A \cdot T^B + C}, \tag{14}$$

the fit-function (see Figure 17) can be used to correct the intensity of each star as long as the effective temperature is available in the used Gaia-catalogue.

By qualitatively inspecting the η_{det} in respect to the peak wavelength on the upper x-axis in Figure 17, this trend is plausible, as the detection is least efficient in longer wavelengths and thereby increasingly effective, the less percentage of the detected spectrum lies in this infrared range.

By correcting the data points (the extraction artifact already straightened out) for this temperature dependent detection efficiency as in Figure 18, the spots gain intensity (as expected).

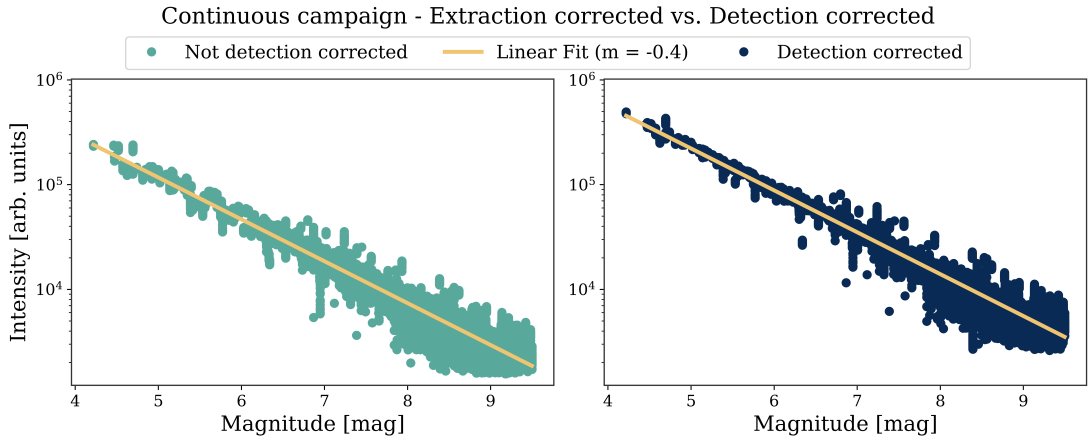

Figure 18: Comparison of data before (left) and after (right) correcting for wavelength depended detection efficiency.

3.3 Extinction Equation

The intensity of a light ray that reaches the observer on the ground depends on three main variables: The initial extraterrestrial intensity outside of the atmosphere I_0, the path-length through the atmosphere (expressed by the airmass X) and the aerosol extinction coefficient of the atmosphere τ. All together they form the extinction equation (Roellinghoff et al., 2025):

$$I = I_0 \cdot e^{-\tau \cdot X}. \tag{15}$$

3.3.1 Calculating the Airmass

The longer the distance a light ray has to travel through the atmosphere, the more intensity it loses. To quantify this, the quantity airmass (X in $[\text{kg m}^{-2}]$) is introduced in atmospherical physics, to describe the effective mass of atmosphere per area a light ray has to cross on its path to the ground. To calculate this X, first an expression for

the path-length s as depending on the zenith distance ($z = 90°$-alt) is created. For this we use the effective height of the atmosphere H, the radius of the earth R_E, the zenith distance to the star z and the entry point where the starlight first hits our atmosphere A. A sketch of the explained variables can be seen in Figure 19.

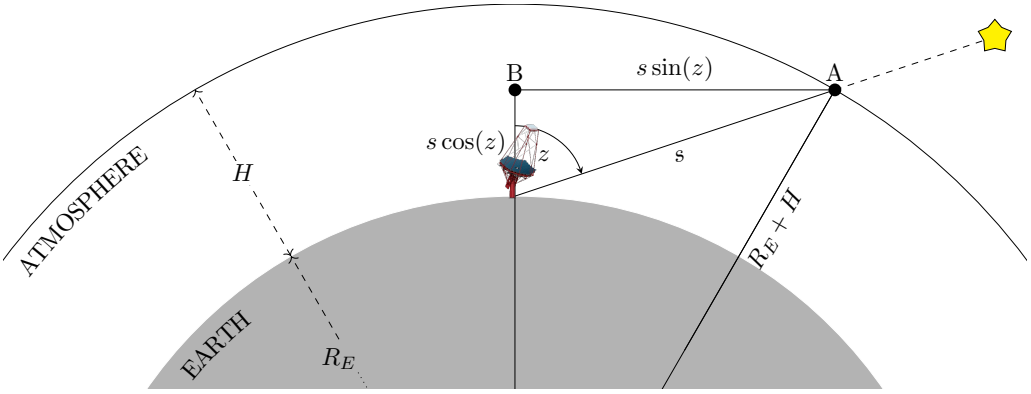

Figure 19: Sketch to calculate the airmass X using the zenith distance z, radius of the earth R_E and the scale height of earth's atmosphere H. Adapted from Wikipedia (2016). MST image credit: CTAO.

Connecting the atmospheric entry point of the starlight A and the telescope site, we get the path length through the atmosphere s, which is to be found. Drawing a right triangle with s as the hypotenuse, the other sides can be expressed by $s\cos(z)$ and $s\sin(z)$. In combination with Earth's centre and radius R_E, a greater right triangle is drawn with the side lengths $R_E + H$, $R_E + s\cos(z)$ and $s\sin(z)$. Using these and the Pythagorean theorem, we can compute s:

$$\begin{aligned}(R_E + H)^2 &= (R_E + s\cos(z))^2 + (s^2\sin(z)^2)\\ 0 &= s^2 + 2sR_E\cos(z) - H^2 - 2R_EH\\ s &= \sqrt{R_E^2\cos(z)^2 + H^2 + 2R_EH} - R_E\cos(z)\end{aligned} \tag{16}$$

This can further be simplified as long as $H \ll R_E$. Since the effective atmospheric height H is modelled by its scale height $H \approx 8.5\,\text{km}$ and the radius of the earth is $R_E \approx 6400\,\text{km}$ (Williams, 2025), this approximation is valid.

This way and with the binomial approximation $\sqrt{1+\epsilon} \approx 1 + \frac{\epsilon}{2}$ (for $\epsilon \ll 1$) the path-length becomes:

$$\begin{aligned}s &\overset{H\ll R_E}{\approx} \sqrt{R_E^2\cos(z)^2 + 2R_EH} - R_E\cos(z)\\ &\overset{\text{binom.}}{\approx} R_E\cos(z)\left(1 + \frac{H}{R_E^2\cos(z)^2}\right) - R_E\cos(z)\\ &= H/\cos(z).\end{aligned} \tag{17}$$

To now construct an expression for the Airmass, we first calculate the Airmass at $z = 0°$:

$$X(z = 0°) = \int_0^H \rho(h)\mathrm{d}h = \rho_0 \int_0^h e^{-h/H}\mathrm{d}h = \rho_0 H \tag{18}$$

with an estimated exponential density distribution $\rho(h)$ and multiply this with the path-length s per zenith-path-length H:

$$X(z) = X(z = 0°) \cdot \frac{s(z)}{H} = \frac{\rho_0 H}{\cos(z)}. \tag{19}$$

The atmospheric density at ground level has a value of $\rho_0 = 1.217\,\mathrm{kg\,m^{-3}}$ (Williams, 2025).

To inspect the dependence of the measured intensity on the zenith distance, the solved exposures of the Pointed Campaign are used, which cover stars in a zenith distance range between 6° and 76°. As this effect is magnitudes smaller than the intensity dependence on the stars' magnitudes, the data is binned by magnitudes (in 0.5 mag steps between 5.0 mag and 9.5 mag) beforehand to generate an even statistic. To visualize possible wavelength dependencies, the stars are further binned by their mean wavelength in 13 equally filled bins (each with 983 data points spread over all magnitudes) between the minimum $\bar{\lambda} \approx 500\,\mathrm{nm}$ and the maximum $\bar{\lambda} \approx 800\,\mathrm{nm}$. Two results for the magnitude

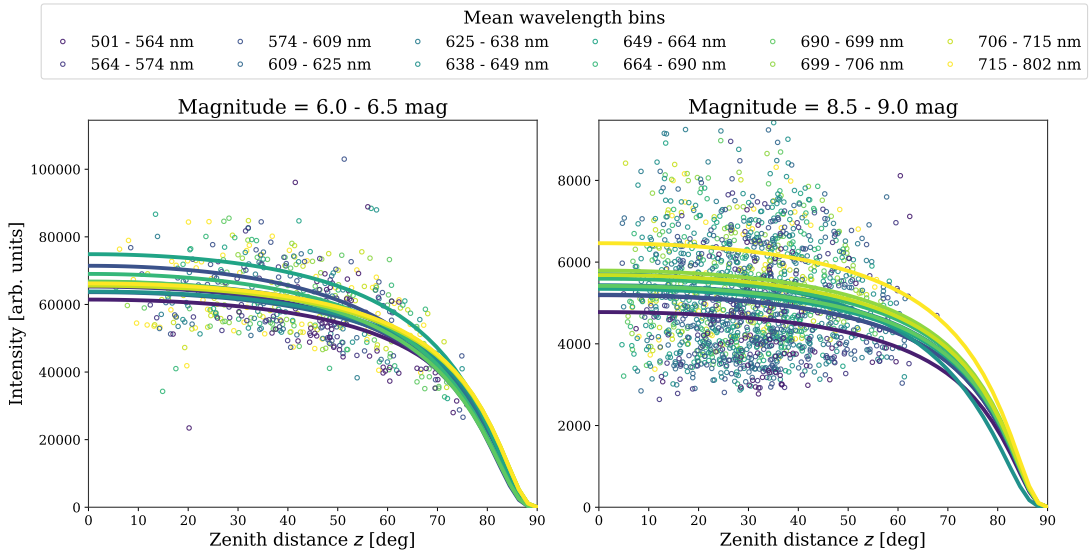

Figure 20: For detection and extraction-efficiency corrected intensity of stars in magnitude ranges 6.0 mag to 6.5 mag and 8.5 mag to 9.0 mag, plotted over the zenith distance ($z = 90°$- altitude). Fitted the extinction equation over zenith distance, binned in 12 mean wavelength bins. Fitted parameters in appendix A.2.3. Remaining magnitude ranges in appendix A.1.1.

ranges 6.0 mag to 6.5 mag and 8.5 mag to 9.0 mag are shown as examples in Figure 20 (the other ones can be viewed in appendix A.1.1). To each $\lambda_{\max}$ bin, in each magnitude bin, the extinction equation (Eck et al., 1999)

$$I_0 \cdot e^{-\tau \cdot X} \tag{20}$$

is fitted, (where X is calculated as constructed in Equation 19), while $\tau(\lambda)$ describes the aerosol extinction coefficient in units of $\mathrm{kg^{-1}m^2}$. To get a representative result, each fit is only done if the $\bar{\lambda}$ bin includes more than 15 data points.

By just looking at Figure 20 one can not make out a trend over different wavelengths, other than the total drop of intensity the closer the stars get to the horizon. The intensity of longer wavelengths neither seems to be consistently higher than the one of shorter wavelengths, nor the opposite is true. The drop rate at higher zenith distances is as well difficult to interpret without corresponding numbers. To make quantitative statements, the fitted values are examined.

3.3.2 Extinction Coefficient τ

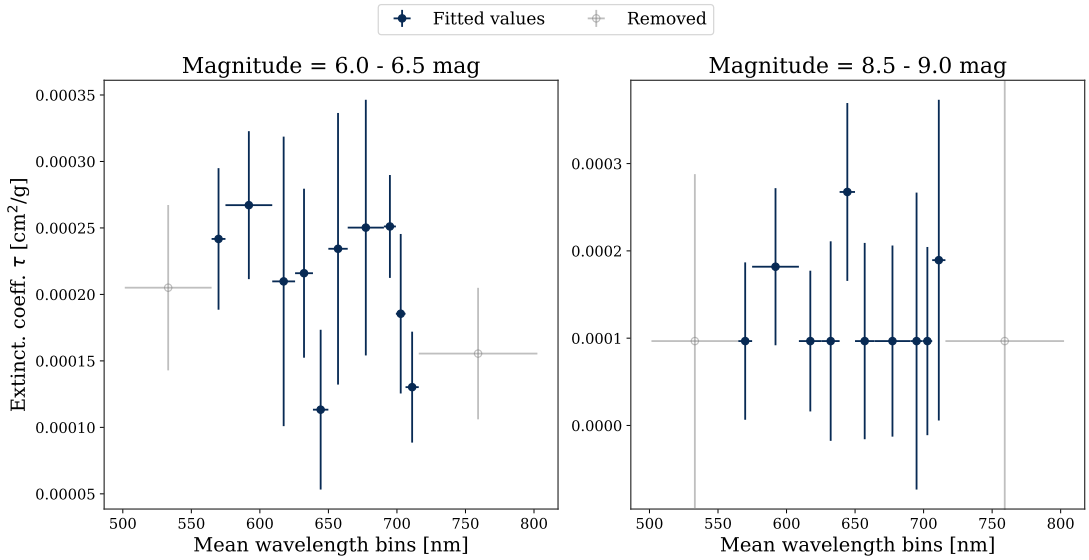

Figure 21: In subsubsection A.1.1 fitted extinction coefficient τ plotted over mean wavelength bins, at two example magnitude ranges 6.0 mag to 6.5 mag and 8.5 mag to 9.0 mag. First and last $^-$ bin removed due to biased edges. Data as fit values in appendix A.2.3. Remaining magnitude ranges in appendix A.1.2.

The fit of the extinction equation provides two fitted values for each $\bar{\lambda}$- and magnitude-bin: The extraterrestrial intensity I_0 and the extinction coefficient τ. We will first take a look at τ by plotting the fitted values over the different $\bar{\lambda}$ bins for each magnitude bin. Two examples for the same magnitude ranges as shown before in Figure 21. All other magnitudes are shown in appendix A.1.2.

Here, the first and last $\bar{\lambda}$ are removed from further analyses as they form the upper and lower edge of the wavelength distribution where only few stars are spread over a large $\bar{\lambda}$ range. To still fill these bins with the same number of datapoints, the width has to increase drastically, which results in an inner distribution far from uniform. This would distort the measurements if not removed.

Even with the two edge bins removed, it is still hard do determine if there is any global trend for the τ dependency on $\bar{\lambda}$, due to the large errors. To resolve this, the mean $\bar{\tau}$, weighted by the fit errors, is calculated for each $\bar{\lambda}$-bin (as in Equation 21) and plotted in Figure 22.

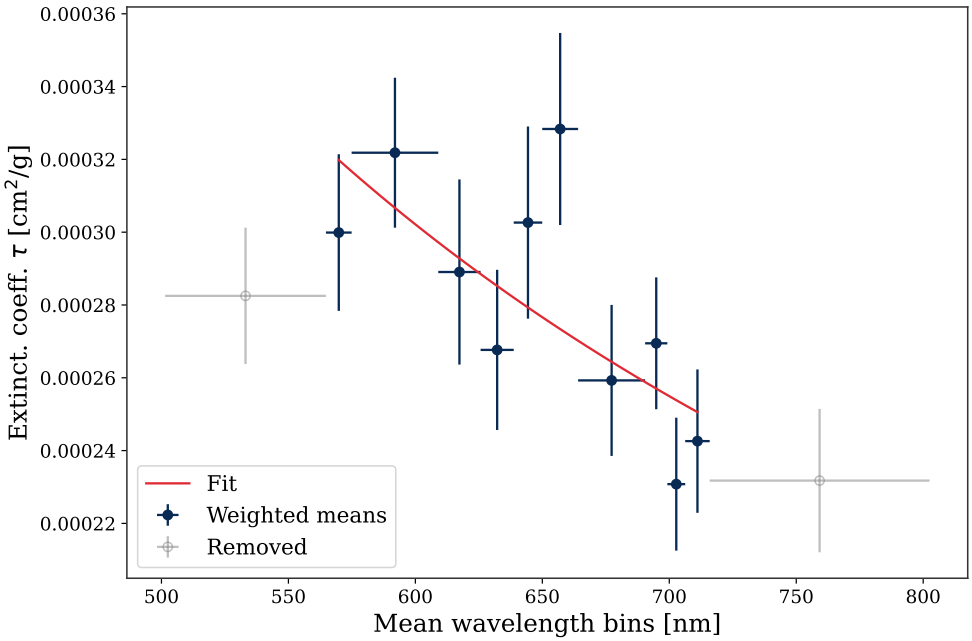

Figure 22: Weighted means (of the aerosol extinction coefficient at different magnitudes) plotted over the corresponding mean wavelength bins. Including an extinction coefficient fit.

$$\bar{\tau} = \frac{\sum \tau \cdot \sigma_\tau^2}{\sum \sigma_\tau^2} \qquad \Delta\bar{\tau} = \sqrt{\frac{1}{\sum \sigma_\tau^2}}. \tag{21}$$

To this $\bar{\tau}$ evolution we fit the expected equation for the aerosol extinction coefficient

$$\tau = \tau_0 \cdot \left(\frac{\lambda}{\lambda_0}\right)^{-\alpha}, \tag{22}$$

where τ_0 is the expected extinction coefficient at a reference wavelength λ_0 and α the Ångstrom exponent. τ_0 quantifies the amount of particles in the air while α can be used as an indicator of the particle size (Schuster et al., 2006).

To get reasonable expectations for the values τ_0 and α the yearly averages by the AERONET station in Mainz are used (M. Andreae, 2023). Mainz is chosen due to its similar geographical, industrial and population conditions to the observation location Erlangen (where no such station is available). 2023 is the most recent year in which data is available for all 12 months, which is why it is chosen as the comparison time span.

With $\lambda_0 = 500\,\text{nm}$ we get a yearly average in Mainz 2023 of $\tau_0 = (1.55 \pm 1.16) \times 10^{-4}\,\text{cm}^2\,\text{g}^{-1}$ and $\alpha = 1.35 \pm 0.37$ (M. Andreae, 2023). As the AERONET catalogue uses the dimensionless optical depth in multiples of the Airmass, the unit got transformed to $\text{cm}^2\,\text{g}^{-1}$, by multiplying the values by ρ_0 and the scale height H.

The fitted values result in the values $\tau_0 = (3.7 \pm 0.4) \times 10^{-4}\,\text{cm}^2\,\text{g}^{-1}$ and $\alpha = 1.10 \pm 0.35$. Thus α as well as τ_0 is located within 1σ of the yearly mean value of a medium sized city.

Therefore the used model for the extinction coefficient τ is interpreted as confirmed.

3.3.3 Extra Terrestrial Flux I_0

The remaining fitted parameter of the extinction equation is I_0 which describes the extraterrestrial intensity a light ray had before entering the atmosphere. The fitted parameter I_0 can now be plotted over the binned magnitudes in Figure 23 to get an estimator for the intensity outside the atmosphere.

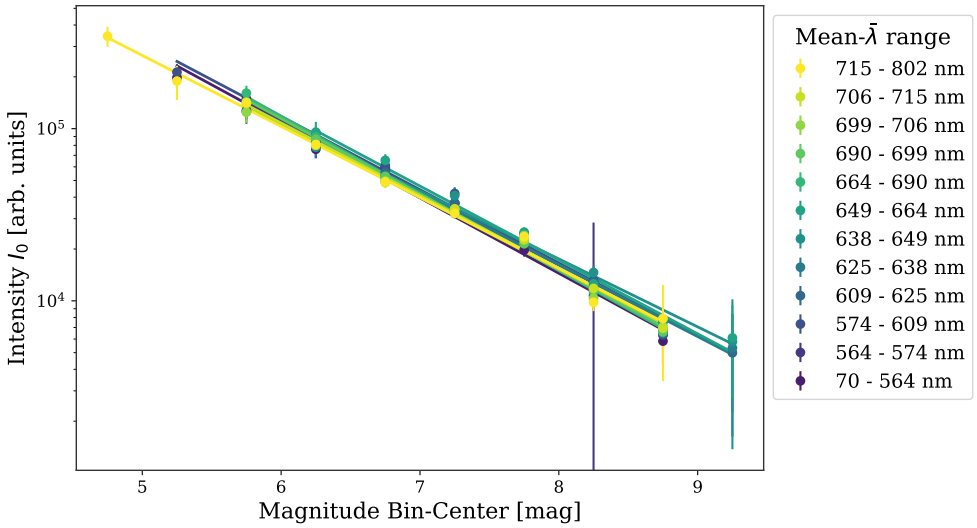

Figure 23: Fitted parameter I_0 of extinction equation at different magnitudes. Exponential fit to data with fitted values in table 7.

As expected, does the extraterrestrial intensity not depend on the wavelength, because I_0 in theory describes the intensity before any wavelength-dependent atmospheric/detection effects have acted on it. The only other extinction a photon at I_0 has already crossed paths with, would be interstellar extinction. This does not need to be taken into account though, as it shifts the catalogued magnitude just as much as the calculated intensity and is, therefore, already factored in.

This is also visible by fitting once again the intensity-magnitude dependency $I = A\exp(-m/2.5\,\text{mag})$ in Figure 23. This results in an average fitted B of $(2.36 \pm 0.08\,)$arb. units/mag. This still lies within a $1.8\,\sigma_B$ range of the theoretical value 2.5 arb.units/mag. The amplitude A averages out to $(41 \pm 9) \times 10^6$ arb units.

To get a function for I_0, all wavelength bins are combined to one I_0 data set, to which the theoretical $I - m$-curve is plotted with the rigid theoretical slope $B = 2.5$arb.units/mag, as expected from the logarithmic definition of the stellar magnitude. This results in an amplitude of $A = (23.4 \pm 0.4) \times 10^6$ arb units. Using this, the extraterrestrial intensity can be calculated for every star.

As I_0 is unaffected by the atmosphere and its processes, the I_0-curve should represent every future campaign the same way. Unfortunately this can not be confirmed or denied at this point in time as there is only one Pointed Campaign currently available. The

fit of the extinction equation needs stars measured over a wide range, and especially at high zenith distances, to create a meaningful fit. The Continuous Campaign only covers a range of $z \approx 16^\circ$ to 35°, which is not sufficient as the intensity drop only really becomes noticeable at $z \gtrsim 45^\circ$ as seen in Figure 20.

4 Predicting the Measured Star Intensity

The previous sections dealt with all the effects that act on a photon beam of a star up until it gets plotted on the screen. By combining the processes described earlier one should be able to predict the measured star intensity for every star where the magnitude (m), the zenith-distance (z) and effective star temperature (T_{eff}) is known, as long as the local extinction variables (τ_0 and α) are known or can be guessed well enough. With enough data points the local values could be estimated for each campaign. The expected detected intensity therefore takes on the form of

$$I_{\text{theo}}(m, z, T) = I_0(m) \cdot e^{-\tau(\bar{\lambda}(T)) \cdot X(z)} \cdot \eta_{\text{det}}(T) \cdot \eta_{\text{extr}}(m). \tag{23}$$

Using the extra terrestrial intensity I_0, the extinction coefficient τ, the Airmass X, the detection and extraction efficiency η_{det} and η_{extr}.

To test if this was done successfully, the predicted star intensity is calculated for every star of the Continuous Campaign and used as a normalizer for the corresponding measured star intensity in Figure 24. Without further limiting the shown y-axis, the

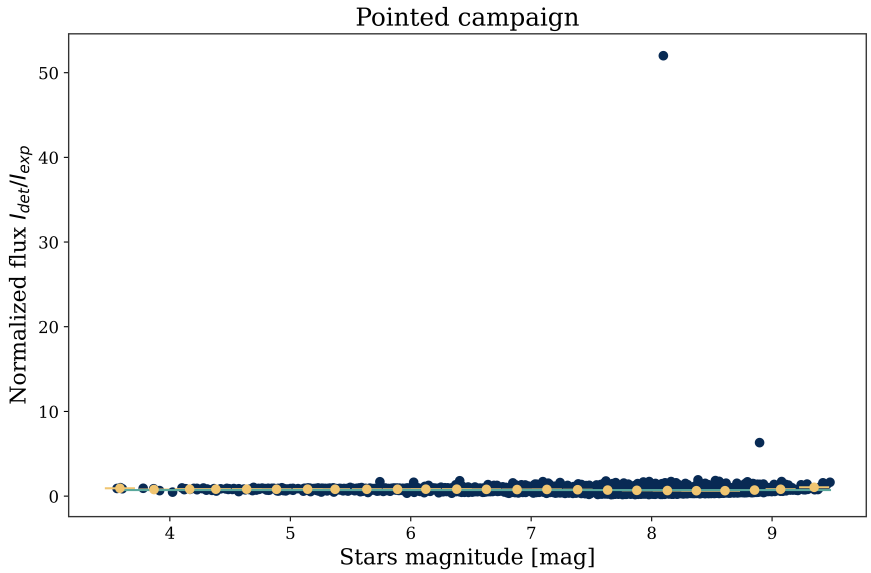

Figure 24: Ratio between detected intensity I_{det} and expected intensity I_{exp} of the Pointed Campaign, binned into 24 magnitude bins (yellow) to track the mean and standard deviation. Two extreme outliers distort view.

data can hardly be seen, as there are two extreme outliers at intensities 7.4 and over 50 times higher than the expected value. As only two spots are affected, and these were already visible before any correction was done, they are no artifact of a wrong estimation. It is likely that they are other objects thana star, that, by chance, aligned in a single frame with the position of a star which led to them getting identified as such.

To get a look at the rest of the data, these extreme outliers are removed from the dataset. The reduced data is shown in Figure 25. As a reference, a horizontal line at $I_{\text{det}}/I_{\text{exp}} = 1$ is included, which symbolizes the expected ratio. To get a better idea of

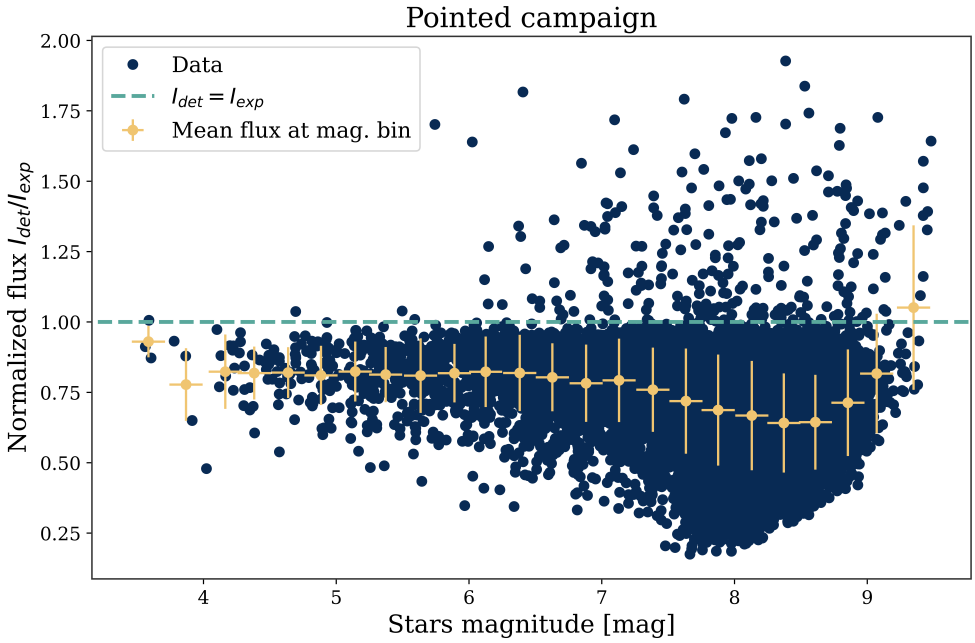

Figure 25: Ratio between detected intensity and predicted, plotted over the corresponding magnitudes. In yellow: Mean normalised flux at each magnitude bin.

the progression, the intensities are binned into 24 magnitude bins by which the mean and standard deviation of each bin are expressed (yellow points).

By looking at Figure 25, the first aspect noticed is the systematic lower intensity as expected. The data seems to nearly completely lie below the prediction, with only the uppermost spots matching the expectation. One explanation could be the neglected interstellar reddening, briefly addressed in section 2. For simplification purposes, we estimate the measured intensity spectrum by the given stellar temperatures. Due to interstellar reddening the spectrum shifts to the reds. As a result, we underestimate the mean wavelength and therefore overestimate the detection efficiency. By this we do not correct enough for the detection and get higher predicted intensities.

4.1 Interstellar Reddening

The interstellar reddening is quantified by $E(B-V)$. $E(B-V)$ is calculated by the difference in magnitude between light in the blue B-band (∼390-490 nm) and the visual bandwidth V (∼ 500-600 nm) (Bessell, 2005; Fitzpatrick, 1998).

As the reddening effect strongly depends on the amount of matter between the star and the observer, the decisive factor is which part of the galaxy is looked at. Because the matter is concentrated in the disc of our galaxy, it is useful to use galactic coordinates. Those are defined by two angles between our sun and the centre of the galaxy. Aligning the galactic disc with our horizontal axis, the angle upwards is called galactic width b, while the angle to the left, looking from the sun to the galactic centre, is called galactic length l (see Figure 26).

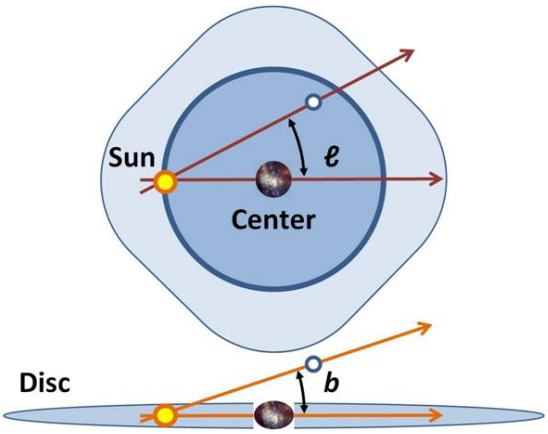

Figure 26: Sketch of the definition of the galactic coordinates b and l. Taken from Wikipedia (2008)

Depending on the composition of the area observed, the reddening factor $E(B-V)$ can vary widely. By, for example, looking directly into the galactic core ($b = l = 0°$), $E(B-V)$ can exceed 80 mag. Just one degree above ($l = 1°, b = 1°$),the value has already dropped to 1.8 mag, at $b = 10°$ it is only around 0.4 mag, and by looking outside the Milky Way ($l = 180°, b = 80°$), we get a mean of 0.01 mag. The catalogued $E(B-V)$ values can be extracted from NASA/IRSA (2013).

The redshifted intensity at a specific wavelength after the ISM $I_{\mathrm{rs}}(\lambda)$ can be predicted by the interstellar extinction equation:

$$I_{\mathrm{rs}}(\lambda) = I_{\mathrm{source}}(\lambda) \cdot 10^{-0.4 A_{\mathrm{ISM}}(\lambda)}, \tag{24}$$

with the original blackbody spectrum I_{peak} and the interstellar visual extinction coefficient A_{ISM} (Fitzpatrick, 1998).

Depending on the area of the galaxy, the stars are located this results in a stronger or weaker shift. As an example, a blackbody spectrum at $T = 30\,000$ K is plotted in Figure 27, with a galactic width in a range of 1° to 50°. The noticeable local minimum at the intensity distribution of $b = 20°$, can be explained by an overlapping of the original peak and the new redshifted peak, since the initial peak is not fully absorbed.

More important is the shift of the dominant wavelength range, which is 15 times higher for $b = 1°$ thanits original value.

Because of this highly regional effect, which has an additional distance dependence, which is not mentioned, it is hard to compensate for it. Especially the pointed campaign covers a wide range of galactic coordinates, which results in $E(B-V)$ values in the range of 0.008 mag to 1.334 mag, with a mean of (0.28 ± 0.39) mag.

In contrast, does the Continuous Campaign observe an area with a mean $E(B-V) = (0.029 \pm 0.017)$ mag. This shows in Figure 28, where the mean detected wavelength fits much better to the predicted value.

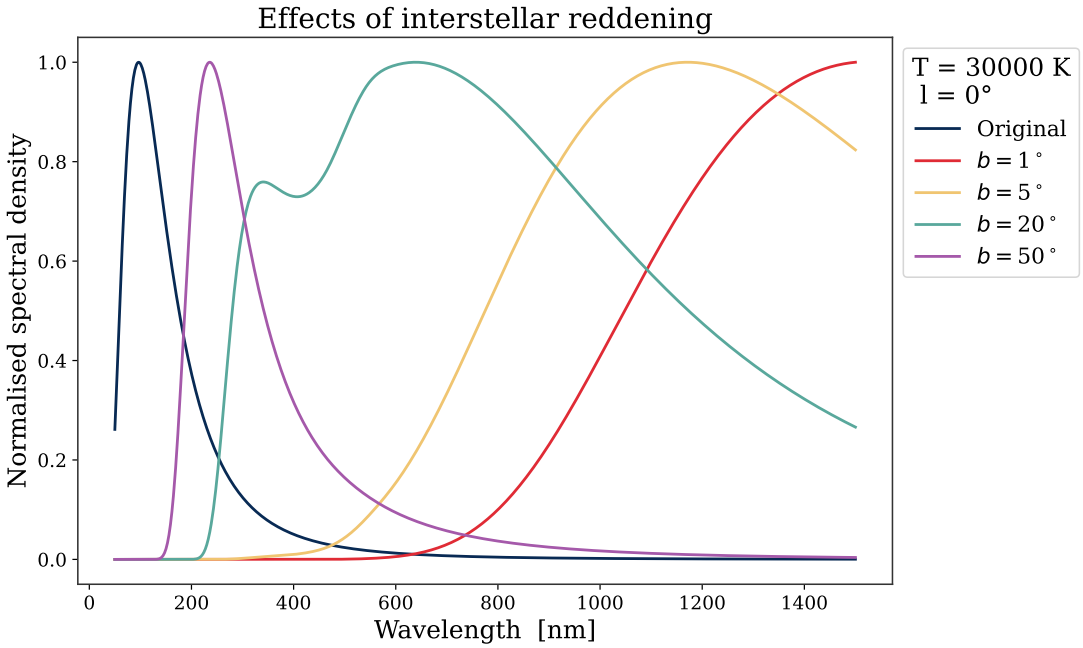

Figure 27: Spectrum of a blackbody with $T = 5000\,\mathrm{K}$, at four different galactic widths. Visible effect: smaller $b \rightarrow$ stronger redshift.

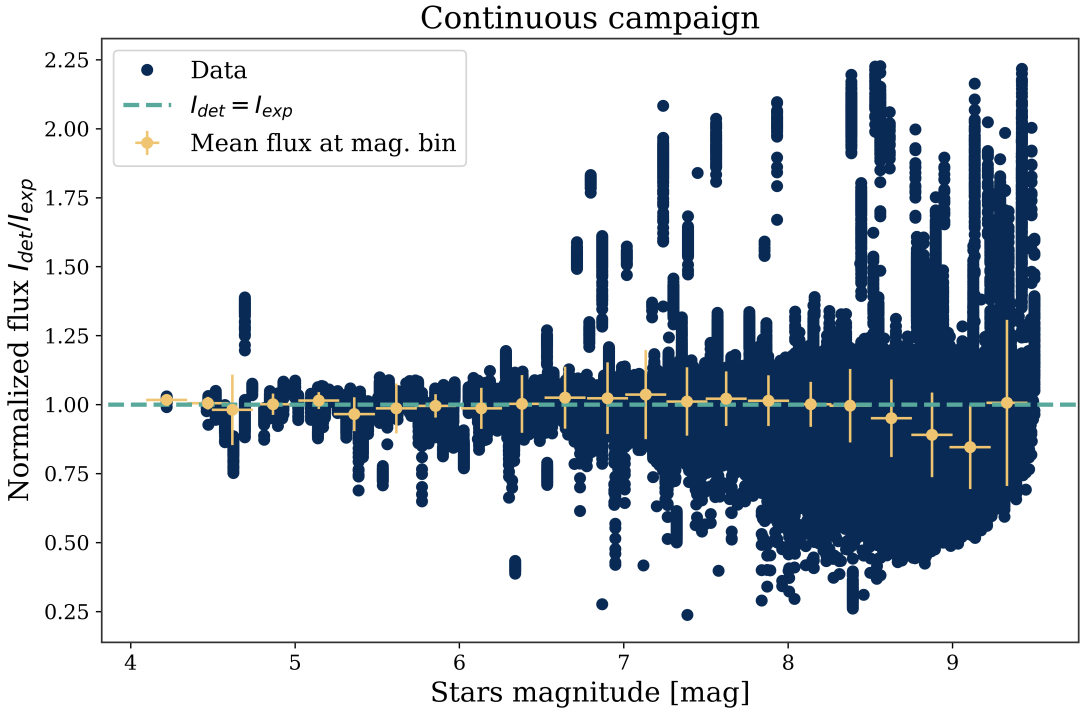

Figure 28: Ratio between detected intensity I_{det} and expected intensity I_{exp}, binned into 24 magnitude bins (yellow) to track the mean and standard deviation.

This strengthens the hypothesis, that the interstellar reddening is the decisive reason for the offset.

Due to time restrictions it is not possible to implement this correction in this thesis, but it is strongly encouraged that this is looked at in future works.

4.2 Removing Badly Fitted Stars

As the Continuous Campaign does not seem to be much influenced by the neglected interstellar reddening, because the campaign pointed out of the Milky Way, it can be used to demonstrate the detection and removing of badly fitted stars.

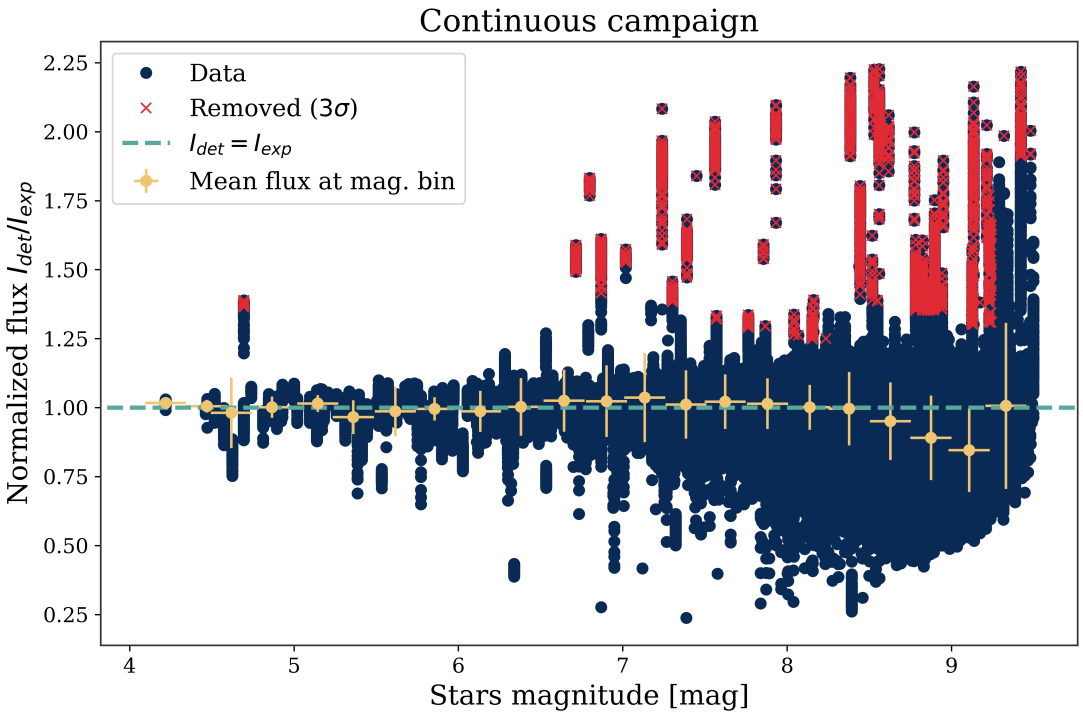

Figure 29: Marked all stars that were detected as wrong fits (outside of 3σ-range) with red x.

As seen in Figure 28 do the mean values follow the expected path consistently within one standard deviation. By calculating the difference to the predicted flux for every star in every bin, in multiples of the corresponding standard deviation in the bin, a selection can be done. Because a star can have a lower intensity than expected, due to for example clouds, a lower star intensity does not necessarily indicate a wrong star match. In contrast, no reasonable explanation can be found to why a star should appear multiple standard deviations brighter than its prediction. According to this consideration a lower threshold can be set, above which all data points are considered wrong matches.

Depending on the number of stars, which might also include correct fits, one wants to remove, the threshold can be set to different values. A 1σ range will statistically discard

32 % of correct data points, 2σ will remove about 95 % and so on. As an example all stars which intensities exceed the 3σ range are marked in Figure 29.

Using the sorted out data set, one could now redo the analysis done in this thesis to get more accurate values, one could also try to analyse if the removed stars have anything in common that led to their wrong identification in the first place or redo the fit with these spots removed to possibly improve the fit quality.

5 Summary and Outlook

A well functioning pointing of CTAO's telescopes is a crucial part for achieving a sufficient modelling and prediction of Cherenkov events. The pointing technique used relies, besides others, heavily on the correct detection and positional reconstruction of stars in PCAM's field of view. A reliable star recognition and differentiation from other bright light sources is decisive for that. By predicting the intensity of a found star and comparison to the measured intensity of the corresponding spot, wrongly assigned stars can be removed and the fit quality improved.

To achieve an intensity prediction, the influences on the measured flux along the beam path were investigated, from the digital spot extraction to the formation of light on the star's surface. The individual corrections contain the:

- systematic flux underestimation for dimmer spots, induced by the extraction algorithm
- wavelength-dependent detection efficiency of the camera composition
- wavelength-dependent atmospheric extinction governed by the path length through the atmosphere and the particles in it

and are dependent on factors in Table 1. In this analysis it was also successfully proven

Effect	Described by	Dependent on
Extraction	η_{extr}	m
Detection	η_{det}	$\bar{\lambda}(T)$
Extinction	I_0, τ, X	m, τ_0, α, z

Table 1: Summary of effects acting on stellar flux. With the extraction and detection efficiencies $\eta_{\text{extr}}, \eta_{\text{det}}$, the extra terrestrial intensity I_0, the atmospheric extinction coefficient τ and the airmass X. With dependencies on the extr. threshold T, magnitude m, mean wavelength in detection range λ_{mean}, reference extinction coeff. τ_0, Ångstrom exponent α and zenith distance z.

that it is possible to measure atmospheric information, such as the Ångstrom exponent and τ_0, which describe the particle sizes and number of particles in the air.

By combining atmospheric information and the other named influences into one equation, it was possible to predict the measured intensity of a star.

While inspecting the $I_{\text{det}}/I_{\text{exp}}$ distribution, a systematic deviation to values < 1 led us to suspect that the interstellar reddening shifts stars' spectra far enough to longer wavelengths, so that the camera detection correction overestimates the efficiency, which leads to lower intensities. The basics of the interstellar reddening were explained briefly, but could not be taken into account.

In future attempts one should definitely quantify and correct for the interstellar reddening. Simultaneously one could use the calculated atmospheric parameters to include the spectral shifting in the atmosphere.

By improving the time efficiency of the algorithm and automating certain processes, the first step would be taken to implement the results of this thesis to the Live-Pointing-Processes of MSTs, to check and improve the fit accuracy on the spot and get atmospheric informations at the array site.

Acronyms

AERONET Aerosol Robotic Network.

AGN Active Galactic Nuclei.

BB blackbody.

Continuous Campaign 2025-03-17 (18:22-03:56 UTC): Continuous night sky campaign on the ECAP rooftop pointed at ALT 65,51°, AZ 1,95°.

CTAO Cherenkov Telescope Array Observatory.

ECAP Erlanger Centre of Astroparticle Physics.

FoV Field of View.

Gaia Global Astrometric Interferometer for Astrophysics.

H.E.S.S. High Energy Stereoscopic System.

ISM Interstellar Medium.

LSTs Large-Sized Telescopes.

MAGIC Major Atmospheric Gamma Imaging Cherenkov Telescope.

MSTs Medium-Sized Telescopes.

PCAM Pointing Camera.

Pointed Campaign 2025-03-20 (19:12-20:16 UTC): Pointed night sky campaign on the ECAP rooftop pointed at 40 different Alt/Az positions.

SSTs Small-Sized Telescopes.

VERITAS Very Energetic Radiation Imaging Telescope Array System.

A Appendix

A.1 Additional Figures

A.1.1 Altitude Dependency

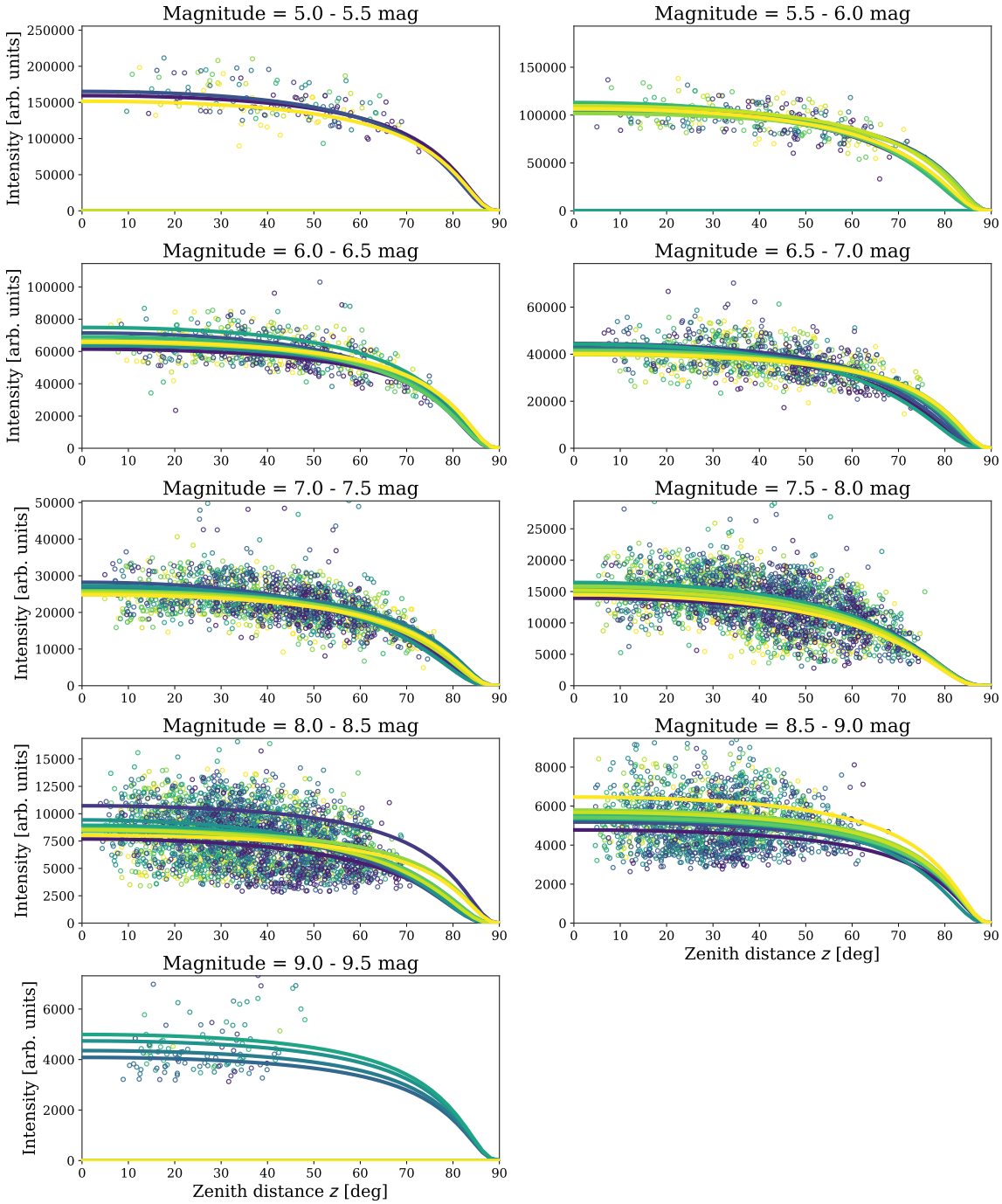

Figure 30: Fitted extinction equation for magnitude bins between 5 mag and 9.5 mag to intensity of stars (binned by their mean wavelength) over the zenith distance z. Fitted variables: I_0 and τ. Fitted parameters in appendix A.2.3.

A.1.2 Extinction Coefficient τ

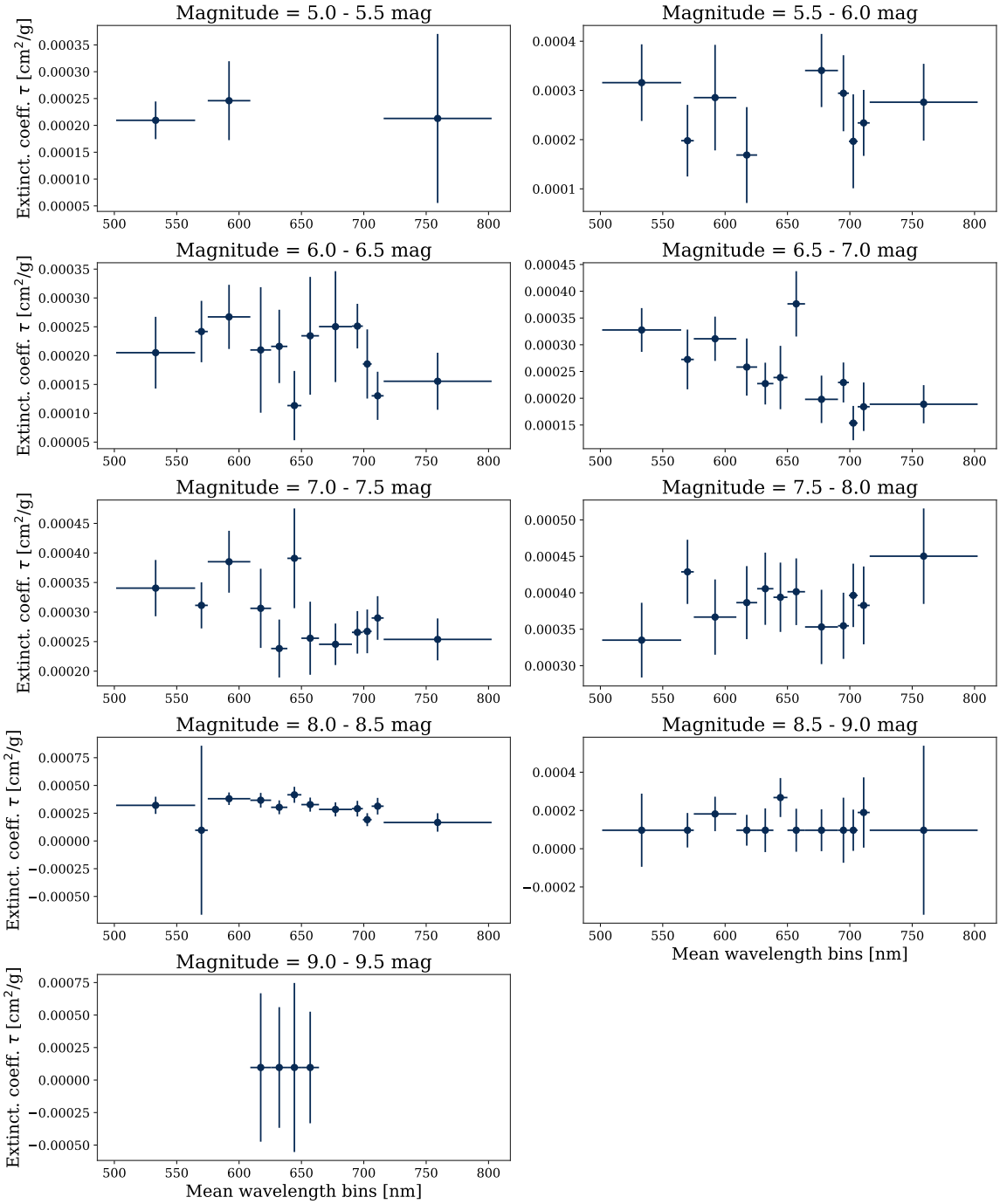

Figure 31: Fitted extinction coefficient τ for magnitude bins between 5 mag and 9.5 mag in appendix A.1.1. Exact values in appendix A.2.3.

A.2 Fit parameters

A.2.1 Extraction and Solving Algorithm

Intensity fit

$I(m) = A \cdot 10^{-m/B} - C$

Plot	$\boldsymbol{A}$ [$\times 10^6$ arb. units]	$\boldsymbol{B}$ [mag]	$\boldsymbol{C}$ [$\times 10^3$ arb. units]
1.0 RMS	8.73 ± 0.12	2.54 ± 0.03	0.91 ± 0.03
5.0 RMS	8.60 ± 0.22	2.57 ± 0.04	9.53 ± 0.16
10.0 RMS	8.46 ± 0.50	2.61 ± 0.08	21.12 ± 0.25

Table 2: Used in Figure 14

A.2.2 Camera Efficiency

Extrapolated Gaussian fit

$\eta_{\text{cam}}(\lambda < 350\,\text{nm}) = \eta_{\max} \exp\left(-\frac{(\lambda-\mu)^2}{2\sigma^2}\right)$

$\boldsymbol{\eta}_{\max}$ [%]	$\boldsymbol{\mu}$ [nm]	$\boldsymbol{\sigma}$ [nm]
91.88 ± 0.12	463.2 ± 1.0	85.7 ± 1.2

Table 3: Used in Figure 16

Extrapolated linear fit

$\eta_{\text{cam}}(\lambda > 1100\,\text{nm}) = m\lambda + t$

$\boldsymbol{m}$ [%/λ]	$\boldsymbol{t}$ [%]
0.050 ± 0.001	55.6 ± 1.9

Table 4: Used in Figure 16

Inverse power fit

$\eta_{\text{det}}(T) = \left(A \cdot T^B + C\right)^{-1}$

$\boldsymbol{A}$ [$\times 10^6 K^{-1}$]	$\boldsymbol{B}$	$\boldsymbol{C}$
8.1 ± 0.5	-1.84 ± 0.07	1.719 ± 0.002

Table 5: Used in Figure 17

A.2.3 Altitude Dependency

Altitude extinction fit

$I = I_0 \cdot \exp(-(z))$

λ_{peak} bin-range [mag]	$\boldsymbol{I_0}$ [$\times 10^3$ arb. units]	$\boldsymbol{\tau}$ [$1/H$]
Magnitude = 5.0 - 5.5 mag		
501 - 564 nm	197.98 ± 12.47	0.22 ± 0.04
564 - 574 nm	$\pm$	$\pm$
574 - 609 nm	213.02 ± 24.55	0.25 ± 0.08
609 - 625 nm	$\pm$	$\pm$
625 - 638 nm	$\pm$	$\pm$
638 - 649 nm	$\pm$	$\pm$
649 - 664 nm	$\pm$	$\pm$
664 - 690 nm	$\pm$	$\pm$
690 - 699 nm	$\pm$	$\pm$
699 - 706 nm	$\pm$	$\pm$
706 - 715 nm	$\pm$	$\pm$
715 - 802 nm	188.99 ± 42.23	0.22 ± 0.16
Magnitude = 5.5 - 6.0 mag		
501 - 564 nm	149.04 ± 19.24	0.33 ± 0.08
564 - 574 nm	127.56 ± 14.60	0.20 ± 0.08
574 - 609 nm	145.19 ± 22.67	0.30 ± 0.11
609 - 625 nm	125.66 ± 19.04	0.20 ± 0.10
625 - 638 nm	$\pm$	$\pm$
638 - 649 nm	$\pm$	$\pm$
649 - 664 nm	$\pm$	$\pm$
664 - 690 nm	160.82 ± 16.84	0.35 ± 0.08
690 - 699 nm	143.73 ± 16.55	0.30 ± 0.08
699 - 706 nm	124.67 ± 16.67	0.20 ± 0.10
706 - 715 nm	139.65 ± 14.17	0.24 ± 0.07
715 - 802 nm	141.72 ± 16.99	0.29 ± 0.08
Magnitude = 6.0 - 6.5 mag		
501 - 564 nm	75.96 ± 8.49	0.21 ± 0.06
564 - 574 nm	83.84 ± 6.50	0.25 ± 0.06
574 - 609 nm	94.18 ± 8.04	0.28 ± 0.06
609 - 625 nm	79.05 ± 11.80	0.22 ± 0.11
625 - 638 nm	83.32 ± 7.73	0.22 ± 0.07
638 - 649 nm	77.96 ± 8.41	0.20 ± 0.07
649 - 664 nm	95.41 ± 14.04	0.24 ± 0.11
664 - 690 nm	89.43 ± 13.42	0.26 ± 0.10
690 - 699 nm	86.60 ± 5.38	0.26 ± 0.04
699 - 706 nm	80.63 ± 7.51	0.20 ± 0.06
706 - 715 nm	80.06 ± 5.39	0.20 ± 0.05
715 - 802 nm	80.91 ± 5.93	0.20 ± 0.05

λ_{peak} bin-range [mag]	$\boldsymbol{I_0}$ [$\times 10^3$ arb. units]	$\boldsymbol{\tau}$ [$1/H$]
Magnitude = 6.5 - 7.0 mag		
501 - 564 nm	59.46 ± 4.13	0.34 ± 0.04
564 - 574 nm	59.00 ± 4.87	0.28 ± 0.06
574 - 609 nm	61.06 ± 4.13	0.32 ± 0.04
609 - 625 nm	55.79 ± 4.35	0.27 ± 0.06
625 - 638 nm	53.58 ± 3.48	0.24 ± 0.04
638 - 649 nm	52.61 ± 4.87	0.25 ± 0.06
649 - 664 nm	65.44 ± 5.57	0.39 ± 0.06
664 - 690 nm	50.15 ± 3.45	0.20 ± 0.05
690 - 699 nm	52.79 ± 2.98	0.24 ± 0.04
699 - 706 nm	49.71 ± 2.63	0.20 ± 0.03
706 - 715 nm	48.64 ± 3.28	0.20 ± 0.05
715 - 802 nm	49.06 ± 2.87	0.20 ± 0.04
Magnitude = 7.0 - 7.5 mag		
501 - 564 nm	37.02 ± 2.81	0.35 ± 0.05
564 - 574 nm	36.93 ± 2.21	0.32 ± 0.04
574 - 609 nm	42.03 ± 3.28	0.40 ± 0.05
609 - 625 nm	36.96 ± 3.48	0.32 ± 0.07
625 - 638 nm	33.85 ± 2.54	0.25 ± 0.05
638 - 649 nm	40.67 ± 4.74	0.40 ± 0.09
649 - 664 nm	33.16 ± 3.01	0.26 ± 0.06
664 - 690 nm	32.17 ± 1.80	0.25 ± 0.04
690 - 699 nm	34.14 ± 1.81	0.27 ± 0.04
699 - 706 nm	33.88 ± 1.88	0.28 ± 0.04
706 - 715 nm	34.20 ± 1.87	0.30 ± 0.04
715 - 802 nm	32.26 ± 1.76	0.26 ± 0.04
Magnitude = 7.5 - 8.0 mag		
501 - 564 nm	19.72 ± 1.64	0.35 ± 0.05
564 - 574 nm	23.12 ± 1.49	0.40 ± 0.04
574 - 609 nm	23.70 ± 1.79	0.38 ± 0.05
609 - 625 nm	23.94 ± 1.72	0.40 ± 0.05
625 - 638 nm	23.81 ± 1.71	0.40 ± 0.05
638 - 649 nm	22.97 ± 1.52	0.40 ± 0.05
649 - 664 nm	24.53 ± 1.62	0.40 ± 0.05
664 - 690 nm	21.47 ± 1.57	0.37 ± 0.05
690 - 699 nm	21.51 ± 1.40	0.37 ± 0.05
699 - 706 nm	23.66 ± 1.44	0.40 ± 0.04
706 - 715 nm	22.63 ± 1.66	0.40 ± 0.06
715 - 802 nm	21.62 ± 1.91	0.40 ± 0.07
Magnitude = 8.0 - 8.5 mag		
501 - 564 nm	10.72 ± 1.26	0.33 ± 0.08
564 - 574 nm	13.10 ± 15.39	0.20 ± 0.84
574 - 609 nm	13.01 ± 1.04	0.39 ± 0.06
609 - 625 nm	12.91 ± 1.16	0.38 ± 0.07

λ_{peak} bin-range [mag]	$\boldsymbol{I_0}$ [$\times 10^3$ arb. units]	$\boldsymbol{\tau}$ [$1/H$]
625 - 638 nm	12.13 ± 1.01	0.31 ± 0.06
638 - 649 nm	14.07 ± 1.31	0.40 ± 0.07
649 - 664 nm	12.54 ± 1.07	0.34 ± 0.07
664 - 690 nm	11.27 ± 0.98	0.29 ± 0.07
690 - 699 nm	11.65 ± 1.07	0.30 ± 0.07
699 - 706 nm	10.35 ± 0.84	0.20 ± 0.06
706 - 715 nm	11.80 ± 1.17	0.32 ± 0.08
715 - 802 nm	9.80 ± 1.09	0.20 ± 0.09
Magnitude = 8.5 - 9.0 mag		
501 - 564 nm	5.83 ± 1.59	0.20 ± 0.21
564 - 574 nm	6.34 ± 0.81	0.20 ± 0.10
574 - 609 nm	6.35 ± 0.75	0.20 ± 0.09
609 - 625 nm	6.56 ± 0.72	0.20 ± 0.09
625 - 638 nm	6.64 ± 0.99	0.20 ± 0.12
638 - 649 nm	7.52 ± 0.95	0.28 ± 0.11
649 - 664 nm	6.53 ± 0.97	0.20 ± 0.12
664 - 690 nm	6.83 ± 0.98	0.20 ± 0.12
690 - 699 nm	6.62 ± 1.40	0.20 ± 0.18
699 - 706 nm	7.07 ± 1.00	0.20 ± 0.12
706 - 715 nm	6.94 ± 1.55	0.20 ± 0.19
715 - 802 nm	7.89 ± 4.47	0.20 ± 0.47
Magnitude = 9.0 - 9.5 mag		
609 - 625 nm	4.99 ± 3.36	0.20 ± 0.61
625 - 638 nm	5.32 ± 3.07	0.20 ± 0.50
638 - 649 nm	5.79 ± 4.41	0.20 ± 0.68
649 - 664 nm	6.10 ± 3.35	0.20 ± 0.47

Table 6: Used in Figure 20 and appendix A.1.1.

$\boldsymbol{I_0}$**-Fit** $I_0 = A \cdot \exp(-\frac{\text{mag}}{B})$		
λ_{peak} bin-range	$\boldsymbol{A}$ [$\times 10^6$ arb. units]	$\boldsymbol{B}$ [mag]
70 - 564 nm	46 ± 15	2.30 ± 0.10
564 - 574 nm	38 ± 16	2.40 ± 0.14
574 - 609 nm	42 ± 14	2.30 ± 0.11
609 - 625 nm	32 ± 9	2.43 ± 0.10
625 - 638 nm	35 ± 12	2.40 ± 0.11
638 - 649 nm	25 ± 9	2.50 ± 0.13
649 - 664 nm	47 ± 22	2.30 ± 0.14
664 - 690 nm	58 ± 10	2.23 ± 0.05
690 - 699 nm	49 ± 8	2.28 ± 0.05
699 - 706 nm	33 ± 12	2.40 ± 0.12
706 - 715 nm	37 ± 9	2.37 ± 0.08
715 - 802 nm	31 ± 7	2.42 ± 0.08

Table 7: Used in Figure 23.

Bibliography

Bessell, Michael S. (2005). "Standard Photometric Systems".
In: *Annual Review of Astronomy and Astrophysics* 43.Volume 43, 2005, pp. 293–336.
DOI: https://doi.org/10.1146/annurev.astro.41.082801.100251.
URL: https://www.annualreviews.org/content/journals/10.1146/annurev.astro.41.082801.100251.

CTAO (2025a). *The Telescopes*.
URL: https://www.ctao.org/emission-to-discovery/telescopes/ (visited on 07/11/2025).

— (2025b). *Venturing Beyond the High-Energy Frontier*.
URL: https://www.ctao.org/emission-to-discovery/science/study-themes/ (visited on 06/03/2025).

Demtröder, Wolfgang (2016). *Experimentalphysik 3. Atome, Moleküle und Festkörper*.
Springer Spektrum Berlin, Heidelberg.
DOI: https://doi.org/10.1007/978-3-662-49094-5.

— (2017). *Experimentalphysik 4. Kern-, Teilchen- und Astrophysik*.
Springer Spektrum Berlin, Heidelberg.
DOI: https://doi.org/10.1007/978-3-662-52884-6.

ECAP (2022). *MST Pointing Camera: Hardware description*.

Eck, Thomas, bullet Holben, Jeffrey Reid, Oleg Dubovik, et al. (1999).
"Wavelength dependence of the optical depth of biomass burning, urban, and desert dust aerosols". In: *J. Geophys. Res.* 104349, pp. 341–344.
DOI: 10.1029/1999JD900923.

Fitzpatrick, Edward (Sept. 1998). "Correcting for the Effects of Interstellar Extinction".
In: *Publications of the Astronomical Society of the Pacific* 111.
DOI: 10.1086/316293.

Gaia Collaboration et al. (2025). *Gaia DR3*.
URL: https://www.cosmos.esa.int/gaia (visited on 06/12/2025).

Garczarczyk, Markus (July 7, 2022).
"Medium-Sized Telescope Structure Technical Design Report".
In: *Version 2.0, MST-STR-TDR-36121000-00001*.

Larsen, Kristian (2025). *Graphreader*.
URL: https://www.graphreader.com/ (visited on 06/12/2025).

M. Andreae, NASA Goddard Space Flight Center (2023).
BAMGOMAS Interactive Tool – Aerosol Synergism Interface.
URL: https://aeronet.gsfc.nasa.gov/cgi-bin/bamgomas_interactive (visited on 07/10/2025).

Matzke, Tina (2024). "Design and characterisation of the Pointing LEDs for the Medium-Sized Telescopes of CTA". Bachelor's Thesis. ECAP, FAU.

NASA/IRSA (2013). *Galactic Dust Reddening and Extinction*. URL: https://irsa.ipac.caltech.edu/applications/DUST/ (visited on 07/10/2025).

Neutelings, Izaak (2025). *Doppler-effect*. URL: https://tikz.net/wave_doppler/ (visited on 07/11/2025).

Roellinghoff, Gerrit, Samuel T. Spencer, and Stefan Funk (2025). *Advanced modelling of Night Sky Background light for Imaging Atmospheric Cherenkov Telescopes*. arXiv: 2505.12895 [astro-ph.IM]. URL: https://arxiv.org/abs/2505.12895.

Rubin, M. (1985). "Optical properties of soda lime silica glasses". In: *Solar Energy Materials* 12.4, pp. 275–288. ISSN: 0165-1633. DOI: https://doi.org/10.1016/0165-1633(85)90052-8. URL: https://www.sciencedirect.com/science/article/pii/0165163385900528.

Schuster, Gregory L., Oleg Dubovik, and Brent N. Holben (2006). "Angstrom exponent and bimodal aerosol size distributions". In: *Journal of Geophysical Research: Atmospheres* 111.D7. DOI: https://doi.org/10.1029/2005JD006328. URL: https://agupubs.onlinelibrary.wiley.com/doi/abs/10.1029/2005JD006328.

Schweizer, Thomas (2025). *Licht ins Dunkel durch Cherenkov-Teleskop Array*. URL: https://www.mpg.de/7832903/mpp_jb_2013 (visited on 07/11/2025).

Suzhou ZWO Co (2025). *ZWO DSO Camera ASI2600MC/MM Pro Product Manual*. URL: https://i.zwoastro.com/wp-content/uploads/2024/07/3d6d8c03e5a8f79c22098e78edcfe5a3.pdf (visited on 06/12/2025).

van Eldik, Christopher (2025). *Offline MST telescope pointing pipeline prototype for CTA (the Cherenkov Telescope Array)*. URL: https://gitlab.com/vaneldik/ctapointing/ (visited on 06/05/2025).

Wikipedia (2008). *The galactic coordinates use the Sun as the origin*. Licence: CC BY-SA 3.0. URL: https://en.wikipedia.org/wiki/Galactic_coordinate_system#/media/File:Galactic_coordinates.JPG (visited on 07/14/2025).

— (2016). *Atmospheric effects on optical transmission can be modelled as if the atmosphere is concentrated in approximately the lower 9 km*. Licence: CC BY-SA 3.0. URL: https://en.wikipedia.org/wiki/Air_mass_(astronomy)#/media/File:Airmass_geometry.png (visited on 07/09/2025).

Williams, David R. (2025). *Earth Fact Sheet*. URL: https://nssdc.gsfc.nasa.gov/planetary/factsheet/earthfact.html (visited on 06/15/2025).

Declaration of Originality

I, Christian Schramm, student registration number: 23025101, hereby confirm that I completed the submitted work independently and without the unauthorized assistance of third parties and without the use of undisclosed and, in particular, unauthorized aids. This work has not been previously submitted in its current form or in a similar form to any other examination authorities and has not been accepted as part of an examination by any other examination authority.

Where the wording has been taken from other people's work or ideas, this has been properly acknowledged and referenced. This also applies to drawings, sketches, diagrams and sources from the Internet.

In particular, I am aware that the use of artificial intelligence is forbidden unless its use an aid has been expressly permitted by the examiner. This applies in particular to chatbots (especially ChatGPT) and such programs in general that can complete the tasks of the examination or parts thereof on my behalf.

Any infringements of the above rules constitute fraud or attempted fraud and shall lead to the examination being graded "fail" ("nicht bestanden").

Place, Date	Signature